Materials for Renewable and Sustainable Energy (2024) 13:109–132
https://doi.org/10.1007/s40243-023-00252-5

REVIEW PAPER

CO_2 photocatalytic reduction with robust and stable metal–organic framework: a review

Ryohei Mori[1,2]

Received: 18 August 2023 / Accepted: 28 December 2023 / Published online: 1 March 2024

Abstract

Climate change and global warming problem are becoming the serious issue and some action is necessary in order to mitigate the rising temperature. CO_2 increase is one of the reason for temperature rise, and the technology to convert CO_2 to beneficial energy or chemical substance could be one of the key solution (CO_2 photocatalytic reduction). Metal–organic frameworks (MOFs) have gained much attention owing to their extremely large surface areas, tunable fine structures, and potential applications in many areas. Recently, MOFs have been demonstrated to be promising materials for CO_2 photocatalytic reduction. This review summarized recent research progresses in photocatalytic reduction using MOFs. MOFs were classified mainly by the type of metal center, and the feature and tendency against their functions towards CO_2 photocatalytic activity will be explained.

Keywords Metal · Organic frameworks · CO_2 photocatalytic reduction · Artificial photosynthesis · Organic ligand

Introduction

Carbon dioxide (CO_2) is a greenhouse gas and one of the major reasons for climate change. In this regard, photocatalytic reduction of CO_2 (the process called "artificial photosynthesis") can produce organic raw materials for fuels and chemicals, from CO_2, water and sun light energy, just like plants. At the same time, they can reduce CO_2 because CO_2 is utilized as raw materials to produce resources for energy and chemicals. Therefore, artificial photosynthesis is said to be one of an ideal green technology [1, 2].

CO_2 photocatalytic reduction, in other words, CO_2 conversion refers to the transformation of CO_2 into valuable products such as fuels and chemicals, which means CO_2 can be utilized directly as a feedstock to react with other components to form chemical products. It should be remembered that CO_2 is a highly stable molecule. As CO_2 molecule, the C–O bond strength in CO_2 molecule is as strong as 364 kJ/mol and the carbon atom has the highest oxidation state. For these reasons, highly efficient catalyst or large energy input is necessary to accelerate CO_2 conversion into valuable chemicals [3]. There exist a few ways to convert CO_2 into valuable energy or chemical products. Those are chemical fixation [4], hydrogenation [5], electrocatalysis [6] and photocatalytic reduction of CO_2 [7, 8].

Among these procedures, photocatalytic reduction and photoreduction of CO_2 gain more attention because this method converts CO_2 into useful energy and chemical products by solely using sustainable solar energy without any extra energy from outside. CO, HCHO, HCOOH, CH_3OH, C_2H_5OH, and CH_4 can be synthesized by this reaction. Chemical substances synthesized by this reaction are determined by the number of electrons and protons transferred in the reactions. The selectivity of product and efficiency of CO_2 reduction are effected by the reaction condition and thermodynamic reduction potentials [9]. Figure 1 presents the schematic figure of photocatalytic reduction of CO_2 reaction steps in a case for a semiconductor with a suitable redox co-catalyst: (i) the semiconductor absorbs light upon irradiation when absorbed light energy is greater than the bandgap of the material, (ii) electron excitation from the valence band (VB) to the conduction band (CB), leaving holes in the VB simultaneously, and (iii) charge migration to the semiconductor particle surface, inducing oxidation reaction in H_2O by the positive holes (h^+), reduction of CO_2

✉ Ryohei Mori
moriryohei@fuji-pigment.co.jp; ryoheimori@gsalliance.co.jp

[1] Green Science Alliance Co., Ltd., 2-22-11 Obana, Kawanishi City, Hyogo Prefecture 666-0015, Japan

[2] Fuji Pigment Co., Ltd., 2-23-2 Obana, Kawanishi City, Hyogo Prefecture 666-0015, Japan

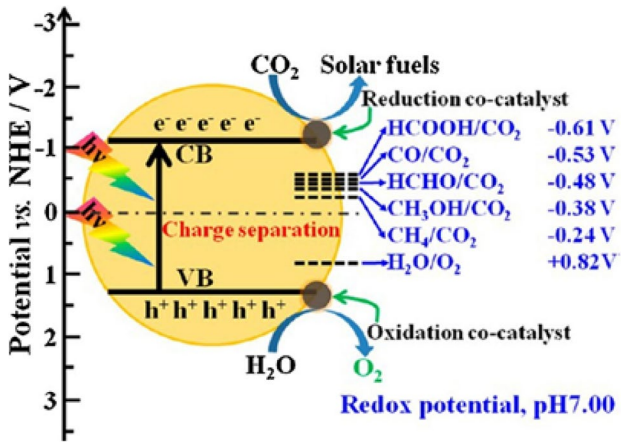

Fig. 1 Elementary steps occurring in a photocatalytic reduction of CO2 over a semiconductor mediated by appropriate redox co-catalysts: i) light absorption, ii) electron excitation from the VB to the CB, iii) charge migration to the surface of the particle, oxidation of H2O by the positive holes (h^+), reduction of CO_2 by multiple electrons (e^-) [14]

Table 1 The photocatalytic reduction reactions of CO_2 in aqueous solution at pH = 7 and their reduction potentials with reference to the normal hydrogen electrode (NHE) at 25 °C and 1 atm

Reaction	E_{eq} (*V* vs SHE)
$CO_2(g)+e^- \rightleftharpoons CO_2^{\bullet-}(aq)$	− 1.99
$CO_2(aq)+e^- \rightleftharpoons CO_2^{\bullet-}(aq)$	− 1.90
$CO_2(g)+2H^+(aq)+2e^- \rightleftharpoons HCO_2H(aq)$	− 0.61
$CO_2(g)+2H^+(aq)+2e^- \rightleftharpoons CO(g)+H_2O(l)$	− 0.52
$3CO_2(g)+H_2O(l)+2e^- \rightleftharpoons CO(g)+2HCO_3^-(aq)$	− 0.56
$CO_2(g)+4H^+(aq)+4e^- \rightleftharpoons H2C(OH)_2(aq)+H_2O(l)$	− 0.49
$CO_2(g)+6H^+(aq)+6e^- \rightleftharpoons CH_3OH(aq)+H_2O(l)$	− 0.38
$CO_2(g)+8H^+(aq)+8e^- \rightleftharpoons CH_4(g)+2H_2O(l)$	− 0.24

by multiple electrons (e^-). The position of the band-edges determines whether or not semiconductors can catalyze and promote a specific reaction. In other words, the position of CB edge has to be more negative than the reaction potential of reduction. Likewise, the VB edge position must be more positive than reaction potential of oxidation [10]. Multiple number of electrons (2–8) required for CO_2 reduction as well as a high recombination rate of electron–hole pairs are the critical issue in photocatalytic CO_2 reduction [11]. Photocatalytic reduction of CO_2 should be reacted either in the gas or liquid phase. In case of the liquid, H_2O is often used as a solvent because it is of low cost and contains rich enough hydrogen. In addition to Fig. 1, the photocatalytic reduction reactions of CO_2 in aqueous solution at pH = 7 and their reduction potentials with reference to the normal hydrogen electrode (NHE) at 25 °C and 1 atm are also exhibited in Table 1 [12, 13].

Various types of photocatalytic materials have been developed including TiO_2 [15], ZnO [16], Fe_2O_3 [17], CdS [18], and ZnS [14]. These are inorganic materials that possess photocatalytic activity mainly under UV light illumination. In contrast, g-C_3N_4 is the one of semiconductor material which can demonstrate photocatalytic activity even under visible-light illumination [19]. Shortcomings of these materials are that their CO_2 adsorption capability is low. Furthermore, high recombination rate of electron–hole pairs is also a concerned issue. On top of that, it is difficult to tune the absorption wavelength of conventional semiconductors because they already have intrinsic bandgap energy. For instance, TiO_2 is mainly used for UV light photocatalysis owing to its own wide bandgap (3–3.2 eV) [20]. ZnO and CdS are not stable in water specially under light illumination, which is preventing them to be applied for actual application usage [21, 22]. Therefore, it is necessary to develop new photocatalytic materials with finely tunable energy band structures, high chemical, and water stability.

Considering above backgrounds, metal–organic framework materials (MOFs) have been gaining much attention recently. MOFs are a promising new generation of adsorbent materials due to their high specific surface area, high porosity, ease of functionalization, and adjustable structure [23, 24]. Compared to weak bonding such as van der Waals bonds and hydrogen bonds, MOFs possess stronger coordination bond energy, which endow them a certain stability. Furthermore, the structure, physical and chemical properties of MOFs are highly customizable; thus, researchers have created more than 20,000 types of MOFs so far, and that number is still growing [25]. This is possible because the use of different center metal ions forms a wide variety of MOF compounds with different organic ligands. As such, the number of possible combination of MOFs is enormous [26]. Various kinds of MOF application are under intensive studies and those include drug delivery systems for biomedical use [27], gas storage and separation [28, 29], catalysis [30], water treatment [31], sensor [32], degradation of organic pollutant [33] and electrochemistry such as batteries and fuel cells [34, 35]. Moreover, MOFs have demonstrated to be promising materials for CO_2 photocatalytic reduction [36, 37]. The mechanism of photocatalytic MOFs is similar to the process of general semiconductors although there are some differences. The VB and CB are represented as the highest occupied molecular orbital (HOMO) and the lowest unoccupied molecular orbital (LUMO) in MOFs, respectively [38, 39]. In case of MOF study in general, the HOMO and LUMO energy levels are correlated with the redox potential energy levels of the organic linker and the metal-oxocluster, respectively [40]. Figure 2 depicts the diagrammatic representation of HOMO/LUMO band of excitation interaction over MOF photocatalyst for CO_2

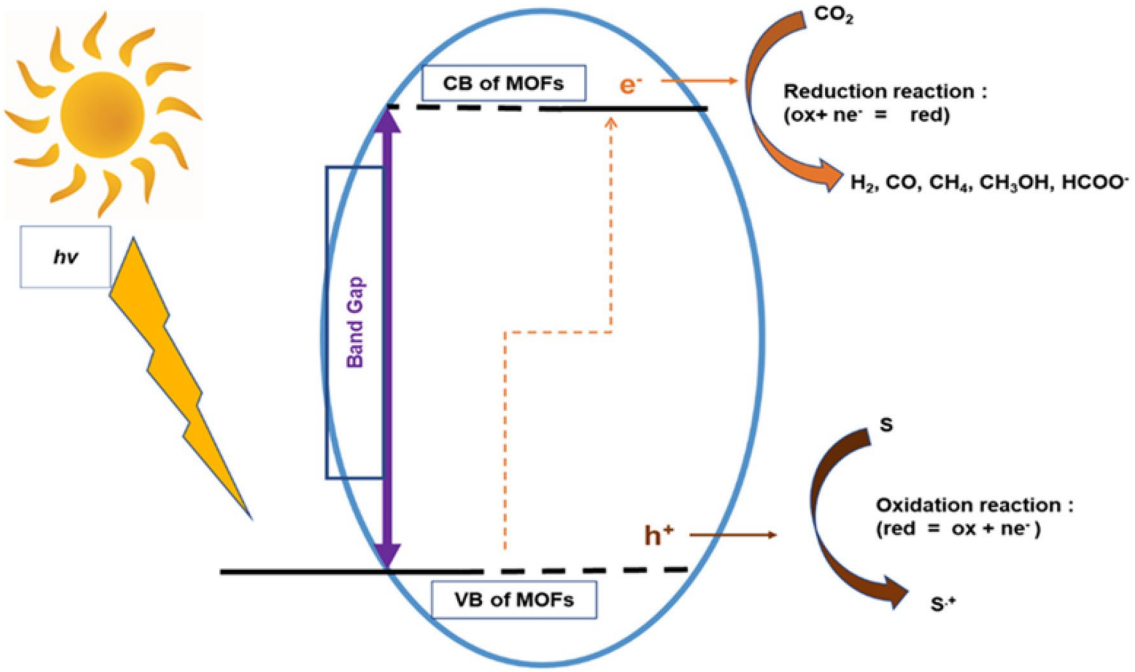

Fig. 2 Diagram of HOMO/LUMO band of excitation interaction over MOF photocatalyst for CO_2 conversion upon light energy irradiation (S = substrate, S^+ = oxidized substrate). HOMO: highly occupied molecular orbital; LUMO: lowest unoccupied molecular orbital; MOF: metal–organic framework; VB: valance bands; CB: conduction band [41]

conversion upon irradiation (S = substrate, S^+ = oxidized substrate). Similar to the above mentioned semiconductor case, photoreduction process is induced upon solar irradiation to initiate the excitation of valence electrons (leaving holes behind) from the HOMO to the LUMO, which are then separated and transported to the MOF surface where the CO_2 reduction is performed [41]. Metal clusters and organic linkers in MOFs can be modified and they can behave as antennas to harvest illuminated light to generate electron–hole pairs for CO_2 photocatalytic reactions. They can be also finely tuned to control the optical absorption range of MOFs. This is also an advantage too. Normally, photocatalytic reactions in MOFs are suggested to be originated from a localized metal-to-ligand charge transfer (MLCT), a ligand-to-metal charge transfer (LMCT), or a π–π^* transition of the aromatic ligand [39].

In addition, as described above, MOFs can be advantageous because they possess extremely large surface area and a high CO_2 adsorption capacity can be expected which is proved experimentally. Owing to this feature, high CO_2 concentration in the pores can enhance the photocatalytic reactions compared to other type of semiconductor. Furthermore, the three-dimensional porous structures and high surface areas enable MOFs to incorporate foreign photoactive species into their frame works, through which photocatalytic reactions can be enhanced by the synergistic cooperation of the metal clusters, organic linkers and the incorporated active sites [42]. It should be noted that some MOFs have an intrinsic catalytic activity resulting from the catalytically active organic linkers and/or unsaturated metal sites [43].

However, in most cases, MOFs can only utilize ultraviolet light and not visible light since most of MOFs are intrinsically active under UV light. To increase light harvesting to visible-light range and to decrease the recombination rate of the photogenerated charge carriers, several challenges have been attempted to enhance MOF photocatalytic activity. Those are optimization of metal and organic linkers, introduction of photocatalytic additive such as metal particles, oxide particles, quantum dot, semiconductors and photosensitizers have been studied to increase photocatalytic activity of MOFs [44–47]. Table 2 summarizes the previous studies of photoreduction reaction of CO_2 with MOFs and MOFs composite materials. MOFs are composed of various types of metal center and organic linkers as well as their composite materials.

However, MOFs are essentially unstable against water and humidity which could be the critical weakness for practical usage. Even though, MOFs based on high valence numbered metal are said to be relatively robust. Thus, in this review, we would like to focus on 4 metals (Fe, Zr, Ti and Al) based MOFs since they are relatively stable against water and humidity [70]. We will also explain the control and modification strategies on the metal cluster, organic ligand of MOFs as well as foreign additive to MOF, and their

Table 2 Summary the previous studies of photoreduction reaction of CO_2 with MOFs and MOFs composite materials

Photocatalyst	Active metal cluster	Organic metal linker	BET (m_2/g)	Photocatalytic reaction condition					Throughput (μmol/g)				Refs.
				Catalyst loading	Solvent	Power	Sacrificial agent	Irradition Time	CO	CH_4	H_2	$HCOO^-$	
ZrPP-1-Co	Zr/Co	THPP	852.3	20 mg	MeCN/TEOA	300-W xenon lamp (λ > 420 nm)	TEOA	15 h	210	7.5			[48]
PCN-136	Zr-O	HCHC	1768				TIPA	12 h					[49]
CsPbBr3 QDs /UiO-66(NH_2)	Zr-O	H_4L	465.7	10 mg	H_2O/ethyl acetate,	300-W xenon arc lamp (λ ≥ 420 nm)	H_2O	12 h	98.57	3.1			[50]
MOF-253-Re-$(CO)_3Cl$	Re–O	dcbpy		5 mg	DMF/H_2O	400 < λ < 800 nm	TEOA	4 h	446		22	1900	[51]
NH2-MIL-101(Fe)	Fe–O	H_4L		2 mg	Solvent-free	300-W xenon arc lamp (400 < λ < 800)	TEOA	5 h	87.6				[52]
NH2-MIL-53(Fe)	Fe–O	H_4L		2 mg	Solvent-free	300-W xenon arc lamp (400 < λ < 800)	TEOA	5 h	15.7				[52]
PCN-222	Zr-O	TCPP	1728	20 mg	MeCN/TEOA	300-W lamp (400 < λ < 800)	TEOA	6 h				2197	[53]
253-Ru(5,50-dcbpy)$(CO)_2Cl_2$	Ru–O	dcbpy		20 mg	MeCN/TEOA	300-W lamp (400 < λ < 800)	TEOA	6 h				2200	[54]
Ir-CP	Ir-ligand	dcbpy		20 mg	MeCN/TEOA	500-W lamp (400 < λ < 800)	TEOA	6 h				2204	[55]
NH2-UiO-66(Zr)	Zr-O	BPDC	778	20 mg	MeCN/TEOA	500-W lamp (400 < λ < 800)	TEOA	6 h				2198	[56]
Eu-Ru(phen)$_3$-MOF	Eu–O	H_3L		20 mg	MeCN/TEOA	300-W lamp (400 < λ < 800)	TEOA	6 h				2205	[57]
co-cat. ZIF-67	Zn–O	TCPP	445	10 mg	MeCN/MeOH/TEOA	300-W xenon arc lamp (400 < λ < 800)	TEOA	6 h	2120		209		[58]
ZMO-550	Zn–O	PTCDA	109.1	100 mg	H_2O	500-W Xenon arc lamp (λ = 400 nm)	TEOA	8 h	126.6				[59]
MOF-74	Zn–O	DHBDC		30 mg	H_2O	500-W xenon lamp		5 h	7.42				[60]
Co6-MOF	Co–O	NTB	1958	3 mg	MeCN/H_2O	150-W xenon lamp (420 ≤ λ ≤ 780)	TEOA	3 h	13.12		9377		[61]
BIF-101	Co–O	NBDC	328.1	10 mg	MeCN/H_2O	λ > 420 nm		10 h	58.3	11			[62]
$Co_{1.11}Te_2 \subset C$	Co-/Te–O	2-mIM	107	1 mg	MeCN/TEOA/H_2O	200-W white LEDs lamp	TEOA	3 h	34.2	73	12.39		[63]
Ni MOLs (Pure CO_2)	Ni–O	BDC	48.9	1 mg	MeCN/TEOA	White LED light (400 nm ≤ λ ≤ 800 nm)	TEOA	2 h	12.5		280		[64]

Table 2 (continued)

Photocatalyst	Active metal cluster	Organic metal linker	BET (m_2/g)	Photocatalytic reaction condition					Throughput (μmol/g)				Refs.
				Catalyst loading	Solvent	Power	Sacrificial agent	Irradition Time	CO	CH_4	H_2	$HCOO^-$	
Ni MOLs (10% dilute CO_2)	Ni–O	BDC	48.9	1 mg	MeCN/TEOA	White LED light (400 nm ≤ λ ≤ 800 nm)	TEOA	2 h	12.5		0.38		[64]
Co-cat. $Ni_3(HITP)_2$	Ni-N4/Ni2 +	HATP	630	2 mg	MeCN/H_2O/TEOA	100-W LED light (λ = 420 nm)	TEOA	3 h	103.5		3745		[65]
O-ZnO/rGO/UiO-66-NH_2	Zr/Zn–O	ATA	877.3	100 mg	$NaHCO_3$ aq	300-W xenon lamp (λ > 420 nm)		6 h				38.5	[66]
4-TiMOF	Zr/Ti–O	BPDC	284	3 mg		150-W xenon lamp (λ > 325 nm)	H_2O	6 h			17.1		[67]
MIL-101—SO_3H	Cr–O	TPA	1937	5 mg	H_2O/TEOA	Light-intensity-controlled xenon lamp	TEOA	10 h	217	13			[68]
MIL-101-Cr	Cr–O	TPA	3127	5 mg	H_2O/TEOA	Light-intensity-controlled xenon lamp	TEOA	10 h	83	17			[68]
MOF-Cu	Cu–O	TCA		5 mg	MeCN/H_2O	300-W xenon lamp (λ ≥ 420 nm)	TIPA	2 h	344		1162		[69]

corresponding photoreduction activities on CO_2. Except aluminum, these MOFs share the similarity that they all contain metal ions with variable valence states (e.g., Fe_3^+/Fe_2^+, Ti_4^+/Ti_3^+ and Zr_4^+/Zr_3^+), which enables their effectiveness on photocatalytic reduction [36]. In addition, Zr, Ti, Al-based MOFs are reported to have relatively large bandgaps such as approximately 3.9 eV, 3.6 eV and 3.4 eV for UiO-66(Zr), MIL-125(Ti) and MIL-53(Al), respectively. Large bandgap ordinary restricts the usage of available solar light energy for photocatalytic activity. Even though, one can improve them to photoresponse to visible-light irradiation by modification of organic linkers, addition of foreign additives such as metal particles, oxide particles as mentioned above. In contrast, Fe-based MOFs intrinsically possess smaller bandgaps such as 1.88–2.88 eV which can respond to visible light without any modification [71].

On top of that, these 4 metals have advantages in terms of material cost and its abundance as natural resource. In the following, we will start with the MOF with iron, which is cheapest and most abundant metal among 4 metals.

Fe-based MOF for CO_2 photocatalytic reduction

In comparison to conventional inorganic semiconductors, it is easier to modify the optical properties and photocatalytic properties of MOFs by optimizing the metal clusters because it is possible by just changing metal resource as raw material. There are some studies demonstrating changing energy bandgap of MOF by shifting the photoabsorption edge from the UV to visible-light region by tuning metal clusters.

So far, Fe, Ti and Zr-based MOFs have been actively investigated photocatalytic MOFs when classified in terms of the metal kind. Fe-based MOF can act as CO_2 photoreduction material because Fe–O clusters can be photoexcited sites to generate electron transfer from O_2^- to Fe_3^+ to form Fe_2^+ even under visible-light irradiation [72]. Since Fe already possess factor as photocatalytic center, Fe-based MOFs can act as photocatalytic material without LMCT reaction [72]. Furthermore, Fe has advantages over material cost and its abundance as natural resource when compared to other metals.

Dao et al. had prepared two types of Fe-based MOFs (MIL-100(Fe) and MIL-101(Fe)) and compared their CO_2 to CH_4 photocatalytic reduction performance. They have found that MIL-100(Fe) demonstrated higher photocatalytic activity and selectivity for CH_4 generation under visible-light irradiation [73].

Three types of Fe-based MOFs, MIL-101(Fe), MIL-53(Fe), and MIL-88B(Fe) were synthesized and compared their photocatalytic activity for CO_2 reduction to form $HCOO^-$ under visible-light irradiation. Photocatalytic

activity of MIL-101(Fe), MIL-53(Fe) and MIL-88B(Fe) of $HCOO^-$ production with TEOA (Triethanolamine) as a sacrificial reactant was 59.0, 29.7, and 9.0 mmol, respectively, with 8 h of visible-light illumination as light energy source. They had clarified that unsaturated Fe sites in structure of MOF were one of the origin for MIL-101 (Fe) to demonstrate the strongest photocatalytic performance. It was deduced that MIL-53(Fe) indicated a higher activity than MIL-88B(Fe) owing to its higher CO_2 adsorption capability (13.5 g/cm^3) than MIL-88B(Fe) (10.4 g/cm^3). Amine functionalization to MOF structure was also speculated to be contributing photocatalytic activity increase since all 3 kinds of Fe-based MOFs exhibited higher activity than the ones without amine functional group.

Two major reasons were proposed for CO_2 photocatalytic enhancement. First, reason was that light energy excitation of organic ligands with amino functional group can accelerate the electron transfer from ligand to Fe center. The other reason was Fe–O cluster can accept direct light energy excitation to cause photocatalytic activity [74].

Experimentally, they had assured visible-light response with UV−VIS spectra. Figure 3 presents the absorbance data of intact MIL-101(Fe) and the one functionalized with NH_2 group. One obvious broadband absorption at 200–450 nm with continued absorption to visible-light region was observed for bare MIL-101 (Fe). One deconvoluted band can be detected at around 270 nm. The band at ca. 270 nm is suggested to be due to charge transfer from the oxygen to iron in an octahedral coordination environment. In addition, existence of Fe_3O clusters contributed to absorption in the visible-light region. Previous studies also demonstrated that the existence of iron clusters in the Fe-based MOF structure can result in light absorption to the visible-light region [75]. Addition of amine group to Mil 101 (Fe) is reported to demonstrate enhanced visible-light response by toluene photodegradation study too [76].

To elucidate the semiconducting properties of MIL-101(Fe) upon light excitation, ESR studies were also carried out to detect the active species involved in the photocatalytic reaction. As shown in Fig. 4, the original reaction system (including MIL-101(Fe) and TEOA) in the dark gives a typical ESR signal ascribed to Fe_3^+ in octahedral FeO_6 [74]. When visible light is irradiated on the above reaction system, the above ESR signal had weakened. This phenomenon can be described by a charge transfer from O_2^- to Fe_3^+ and the evolution of Fe_2^+ in MIL-101(Fe) by visible-light irradiation. When CO_2 concentration was increased again by adding extra CO_2 into experimental setup, ESR signal of Fe_3^+ was emerged again. This indicates that the photogenerated Fe_2^+ is necessary in the photocatalytic CO_2 reduction [77].

Photocatalytic CO_2 reduction reaction without any solvent and liquid was carried out and experimental setup is illustrated in Fig. 5 [52]. A few kinds of Fe-based MOF were prepared and amino functional group was also introduced to extend light absorption to visible-light range. In their experiment, MOF was uniformly and evenly spread onto a glass fiber film as a substrate and utilized as photocatalytic reaction sites. Then, the CO_2 gas was pumped into experimental apparatus in order to initiate the reaction. Sun et al. had proposed that this type of liquid free CO_2 photocatalytic reduction system would be more ideal for real application usage since contact area of CO_2 gas and catalytic part can be enlarged easily, when compared to conventional liquid–solid reaction artificial photosynthesis system.

To investigate more detail of CO_2 photocatalytic reaction mechanism with Fe-MOFs, semiconductor behaviors of the Fe-MOFs were analyzed with UV–Vis spectra

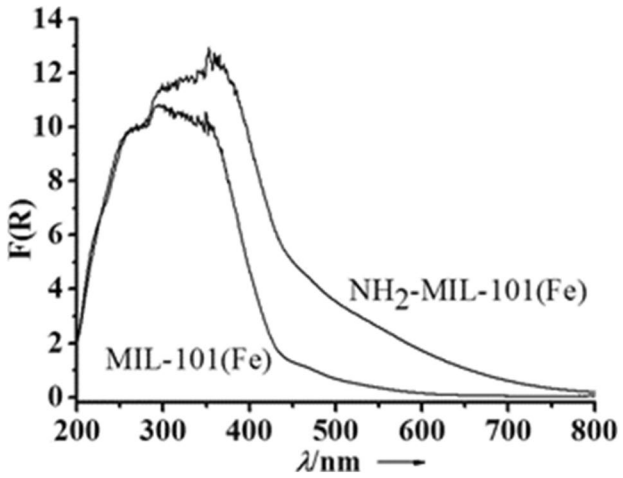

Fig. 3 UV–Vis spectra of MIL-101(Fe) and NH_2 Mil 101 (Fe) [74]

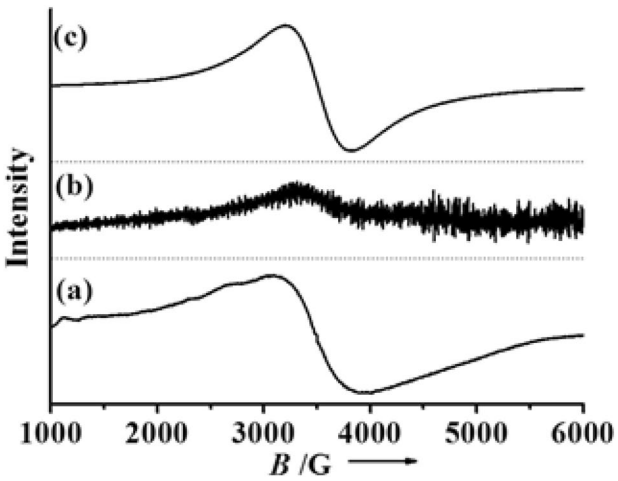

Fig. 4 ESR spectra of a MIL-101(Fe) and TEOA mixture [74]. **a** In the dark, **b** light irradiation, **c** in the presence of CO_2 with light irradiation

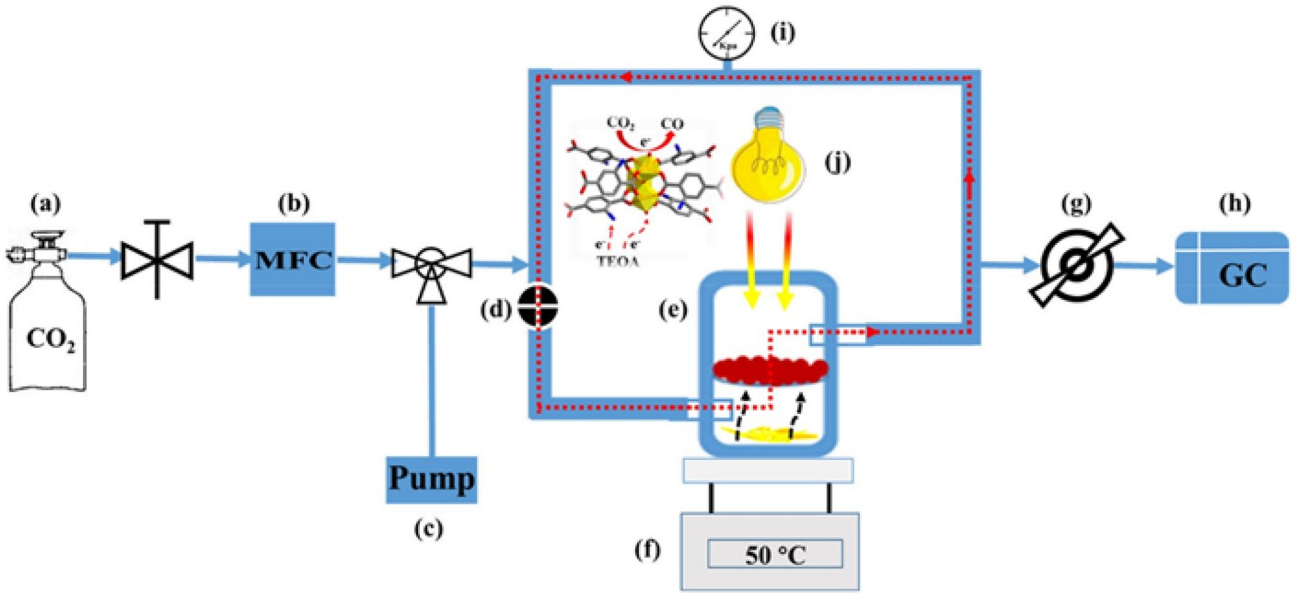

Fig. 5 Experimental setup illustration for the solvent free CO_2 photocatalytic reduction reaction [52]. **a** CO_2 steel cylinder **b** mass flow controlled, **c** vacuum pump, **d** circulating pump, **e** photoreactor, **f** heating plate, **g** automatic gas sampler, **h** gas chromatograph, **i** pressure meter, **j** light source

and Mott−Schottky electrochemical measurements. With Mott−Schottky method, bandgap energy can be calculated out by intercept of the tangents of $(Ahυ)^2$ vs photon energy, in which A is a constant and υ is the incident photon energy [48]. As a results, the bandgap energy was estimated to be 1.98, 1.72, and 1.77 eV for NH_2-MIL-53(Fe), NH_2-MIL-88B(Fe), and NH_2-MIL-101(Fe), respectively (Fig. 6a). Since the metal cluster environment including coordination number is similar for NH_2-MIL-88B(Fe) and NH_2-MIL-101(Fe), they would possess similar bandgap energy as well as the flat-band potentials. Photoluminescence (PL) spectra of Fe-MOFs are measured with 350 nm excitation light (Fig. 6b). One can clearly observe that NH_2-BDC (terephthalic acid) ligand exhibit emission at 485 nm. When metal–organic framework was combined, this obvious emission was disappeared and Fe-MOFs exhibited lower fluorescence. This phenomenon can be explained with ligand-to-metal charge transfer (LMCT) due to the combination of organic groups and the metal–organic framework [52].

The photocurrent measurements were performed in order to clarify the photogenerated charge separation efficiency. In general, higher photocurrent is the proof of higher photocatalytic activity [78]. The result of Fig. 6c deduces that the NH_2-MIL-101(Fe) possesses the highest photocurrent and photocatalytic activity among the Fe-MOFs. Thus, NH_2-MIL-101(Fe) is suggested to have the strongest CO_2 photocatalytic reduction activity.

Furthermore, electrochemical impedance spectroscopy (EIS) was measured to elucidate the carrier mobility of Fe-MOFs (Fig. 6d) [52]. NH_2-MIL-101(Fe) exhibited the lowest impedance which suggests the most efficient charge transfer among Fe-MOFs. The conductivities were calculated out from the Nyquist plots results by applying equation, $\sigma = L/(S \times Ret)$, in which L (cm) and S (cm_2) are the thickness and area of the sample, respectively. It is known that the electron transfer resistance (Ret) is equal to the semicircle diameter in the Nyquist plots [79]. As a result, NH_2-MIL-101(Fe) demonstrated a highest conductivity of 4.1×10^{-6} S cm_{-1} compared to those of NH_2-MIL-53(Fe) and NH_2-MIL-88B(Fe) with conductivities of 1.1×10^{-6} and 2.2×10^{-6} S cm_{-1}, respectively. Conductivity difference can be described by their framework structures. Regarding NH_2-MIL-101(Fe), four μ3-O-bridged Fe_3O clusters exist in a tetrahedron form (Fig. 7c). In this case, electron can move around easier than the case in the triangular bipyramidal form of five Fe_3O clusters in NH_2-MIL-88B(Fe) (Fig. 7b). Furthermore, NH_2-MIL-53(Fe) with μ2-OH bridges (Fig. 7a) indicated lower conductivity than NH_2-MIL-88B(Fe) and NH_2-MIL-101(Fe). So that as speculated from photocurrent measurement, NH_2-MIL-101(Fe) should have the strongest CO_2 photocatalytic activity.

Besides looking at functional group conjugation and iron cluster environment in MOF structure, addition of foreign substance such as quantum dot was investigated. Lu et al. attempted preparing quantum dot–MOF composite material. Iron-based MOF with quantum dot (QD) was synthesized as efficient CO_2 photocatalytic material. They encapsulate $CH_3NH_3PbI_3$ ($MAPbI_3$) perovskite QDs in the pores of Fe porphyrin-based MOF PCN-221(Fe_x)

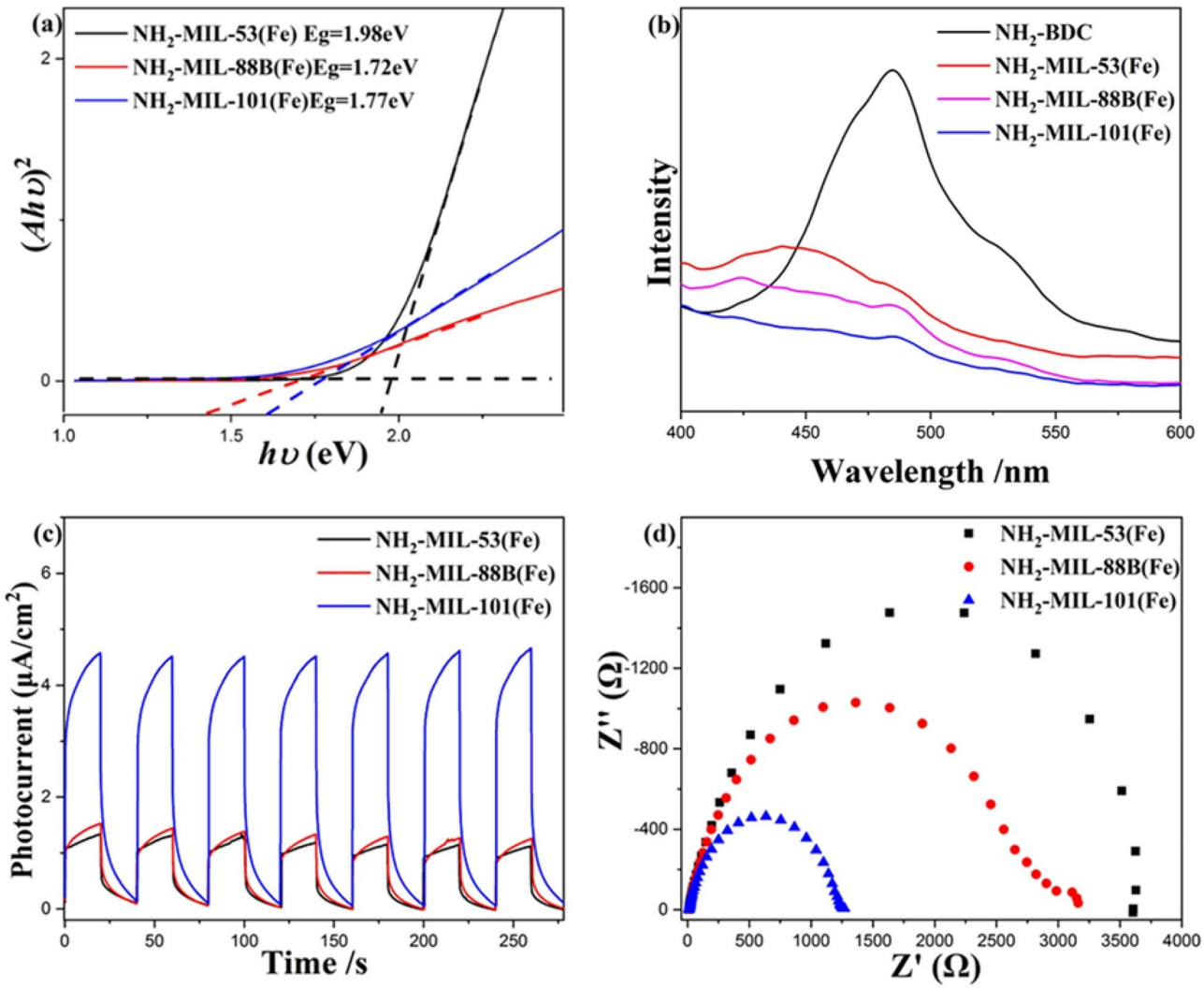

Fig. 6 **a** Plots of $(Ahv)_2$ vs photon energy. **b** PL emission spectra ($\lambda_{ex} = 350$ nm). **c** Photocurrent responses. **d** EIS Nyquist plots for NH_2-MIL-53(Fe), NH_2-MIL-88B(Fe) and NH_2-MIL-101(Fe)

($x = 0 - 1$). Stability of QD was largely enhanced even in a water by synthesizing MOF-QD composite. They also discovered that the close contact of QD next to the iron increased the catalytic reaction by transferring photogenerated electrons to Fe catalytic site rapidly. Prepared composite material exhibited 38 times higher CO_2 photocatalytic activity compared to the MOF without perovskite QD (PCN-221($Fe_{0.2}$)). To further elucidate the reason of largely improved photocatalytic CO_2 reduction reaction, they investigated the light-harvesting property of MOF-QD composite materials by measuring the electronic absorption spectra of $MAPbI_3$@PCN-221($Fe_{0.2}$) and PCN-221($Fe_{0.2}$)). They proved that the absorption strength of $MAPbI_3$@PCN-221(Fe0.2) was superior than that of PCN-221($Fe_{0.2}$) which should be due to high absorption coefficient of quantum dot.

Flat band potentials were calculated out from Mott–Schottky plots. In addition, results were approximately 1.00 V and 1.25 V (against the normal hydrogen electrode (NHE)) for PCN-221($Fe_{0.2}$) and $MAPbI_3$@PCN-221($Fe_{0.2}$), respectively (Fig. 8a, b). From these results, one can say that photogenerated electrons in PCN-221($Fe_{0.2}$) is strong enough to reduce CO_2 to CO (@0.52 V vs. NHE) or CH_4 (@0.24 V vs. NHE). Furthermore, the transfer of photoexcited electron in QD-MOF composite to MOF is thermodynamically possible. Therefore, photoinduced electrons could transfer from porphyrin and $MAPbI_3$ QDs to Fe catalytic sites.

They have additionally performed the steady-state photoluminescence (PL) measurements to scrutinize the photogenerated electron behavior in QD-MOF composite. PCN-221 exhibited 2 obvious peaks around 655 and 712 nm and

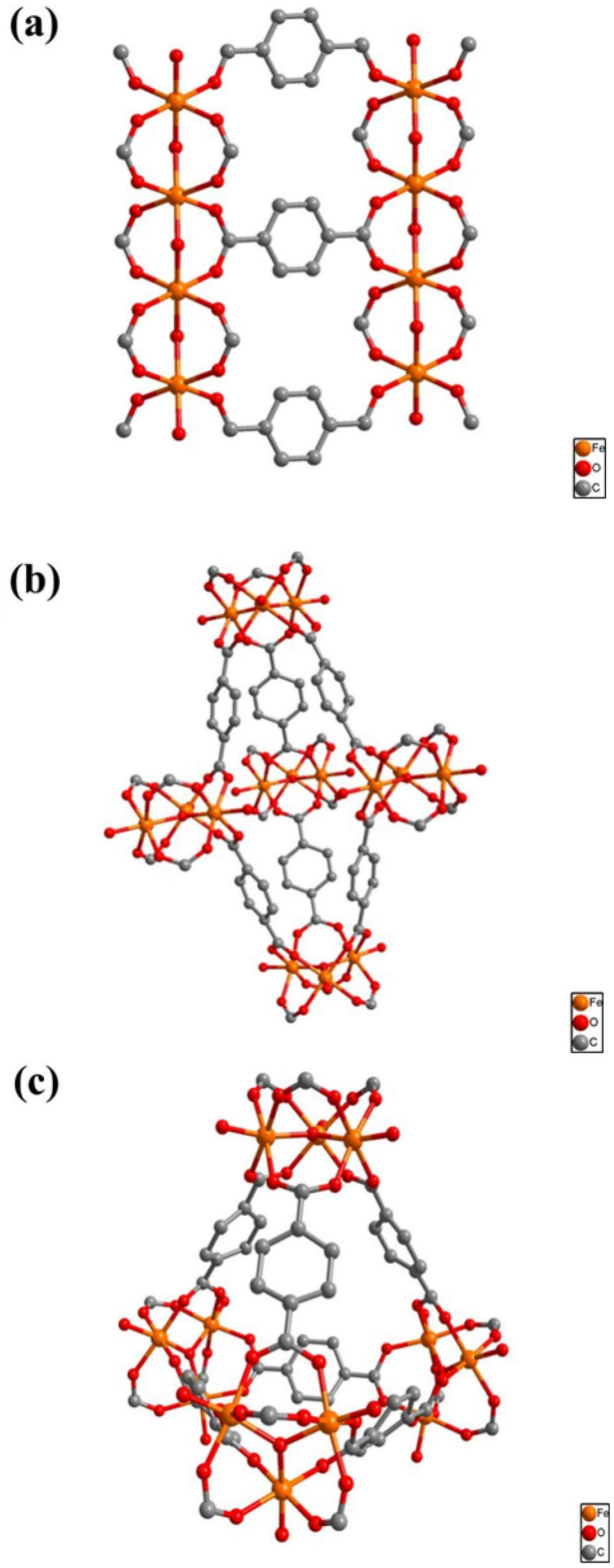

Fig. 7 Structures of Fe-MOFs NH_2-MIL-53(Fe) (**a**) NH_2-MIL-88B(Fe), (**b**) NH_2-MIL-101(Fe) (**c**)

they are suggested to be arise from PL of porphyrin groups. New peak appears approximately at 610 nm when $MAPbI_3$ QD is combined. This is obviously due to QD itself luminescence. However, when Fe is combined in case for PCN-221($Fe_{0.2}$) and MAPbI3@PCN-221($Fe_{0.2}$), all of these peaks disappears. This is because efficient transfer of photogenerated electrons occurs from porphyrin and quantum dot to Fe catalytic sites.

Time-resolved photoluminescence (PL) was carried out in order to speculate the photoexcited charge separation dynamics. Figure 8d shows a rapid PL decay in PCN-221($Fe_{0.2}$) compared to PCN-221 which is without Fe ion. This fact indicates the rapid electron transfer from porphyrin groups to Fe catalytic sites is proceeding after electrons are generated by photoexcitation. In addition, $MAPbI_3$@PCN-221($Fe_{0.2}$) also presented a fast PL decay compared to PCN-221($Fe_{0.2),}$ indicating the same phenomenon is happening from $MAPbI_3$ QDs to Fe catalytic sites, instead of porphyrin group to iron. Thus, it was suggested that this is due to the close contract between $MAPbI_3$ QDs and Fe catalytic sites [80].

Among Fe-based MOF materials, MIL-101(Fe) exhibited the strongest CO_2 photoreduction activity owing to unsaturated Fe sites in its structure. The existence of Fe_3O clusters in MIL-101(Fe) is the main origin of visible-light photocatalytic response although it was further enhanced by addition of functional amine group to organic linker, by accelerating the electron transfer from ligand to Fe center. In addition, it was clarified that high conductivity of NH_2-MIL-101(Fe) also contributed the strong photocatalytic activity which is due to fast electron transfer in four μ3-O-bridged Fe_3O clusters exist in its tetrahedron form. MOF–quantum dot composite material had stronger CO_2 photoreduction activity than bare MOF because of the close existence of quantum dot adjacent to the iron. Photogenerated electrons were efficiently transferred from porphyrin groups as MOF organic linker, to Fe catalytic site, via quantum dot. Stronger light absorption ability of MOF quantum dot composite material was another reason for improved CO_2 photoreduction reaction.

Zr-based MOF for CO_2 photocatalytic reduction

Zr has 4 valence numbers and its high valence number can confer Zr-based metal–organic framework to possess high stability against surrounding environment especially against water and humidity. They also bear strong robust framework, structures and high chemical, thermal stabilities [81]. UiO-66(Zr) and UiO-67(Zr) are the representative type of Zr-based MOFs and composed of $Zr_6O_4(OH)_4$ SBUs (Secondary Building Unite) with BDC ligands and

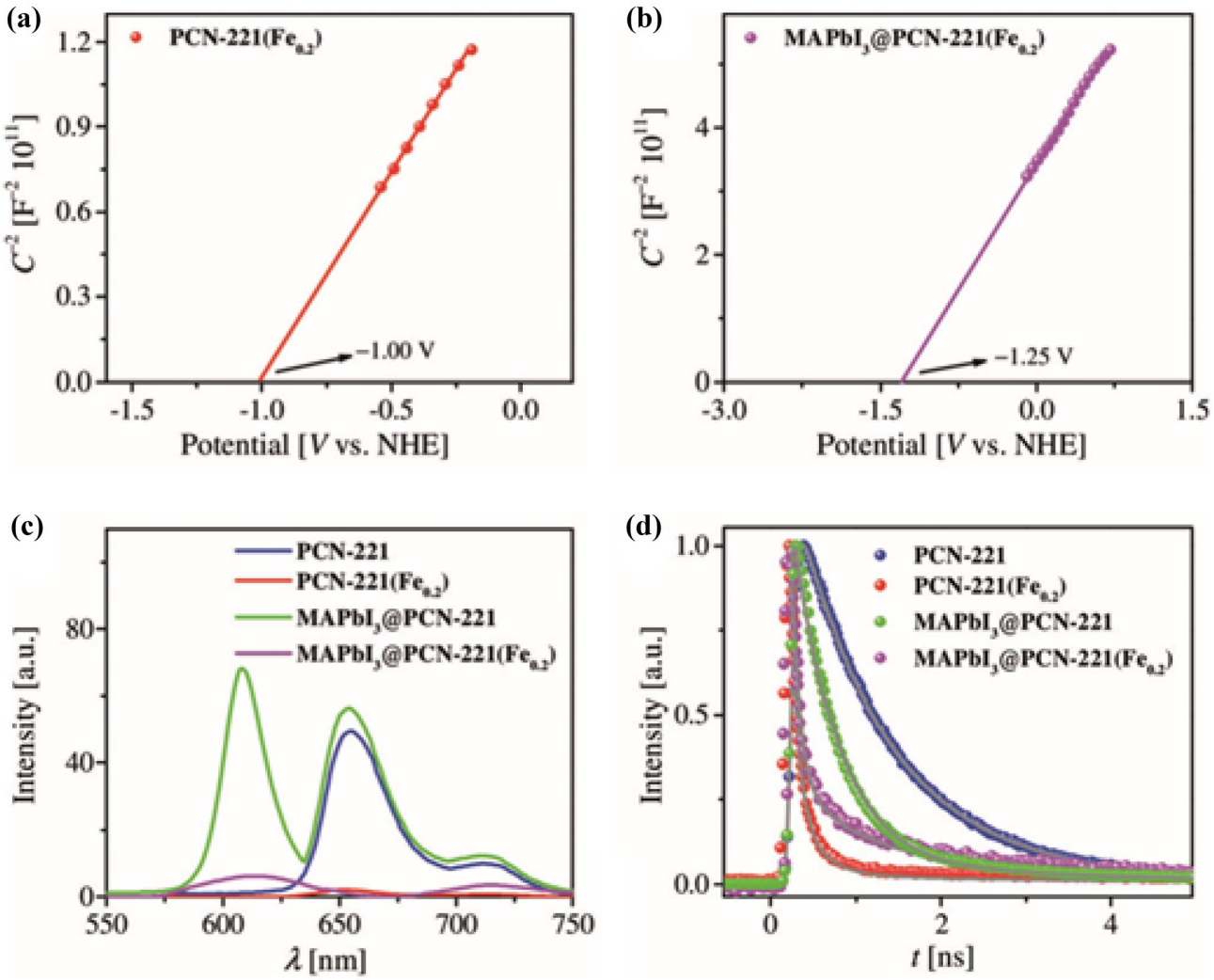

Fig. 8 **a** Mott–Schottky plots of PCN-221($Fe_{0.2}$) and **b** $MAPbI_3$/PCN-221($Fe_{0.2}$). **c** Steady-state photoluminescence spectra of PCN-221, PCN-221($Fe_{0.2}$), $MAPbI_3$/PCN-221, and $MAPbI_3$/PCN-221(Fe0.2). **d** Time-resolved photoluminescence decays of PCN-221, PCN-221($Fe_{0.2}$), $MAPbI_3$/PCN-221, and $MAPbI_3$/PCN-221($Fe_{0.2}$) with ET519LP as long-wavelength pass filter, after excitation at 375 nm

4,4′-biphenyldicarboxylic acid (BPDC) ligands, respectively [82]. There are some study carrying out CO_2 photocatalytic reaction with these stable zirconium-based MOFs.

Liu et al. synthesized two metal ion (Co_2^+, Re^+) doped UiO-67 as catalysts for the photocatalytic CO_2 reduction and presented that Cobalt-doped UiO-67 indicated stronger CO_2 photocatalytic activity compared to Rhenium-doped UiO-67. Higher CO_2 absorption capacity and charge carrier mobility are suggested to be the reason for Co-UiO-67 to exhibit stronger CO_2 photocatalytic activity than Re-UiO-67. It was also elucidated that energy barrier of Re-UiO-67 (0.92 eV) for photocatalytic reaction from CO_2 to CO turned out to be higher than that of Co-UiO-67 (0.86 eV) by density functional theory (DFT) calculation. Since energy barrier of cobalt-doped MOF was lower, one could deduce that Co-UiO-67 exhibited stronger CO_2 photocatalytic activity [83].

Conjugation of amine functional group onto MOFs is one of major strategy to extend its light response to longer wavelength. Sun et al. had synthesized zirconium metal–organic framework Zr-SDCA-NH_2, (SDCT: stilbenedicarboxylic acid). Since this material is zirconium metal-based MOF, it exhibited high chemical stability and light absorption edge was extended to around 600 nm. The CO_2 photoreduction ability as formate formation rate of prepared amine conjugated zirconium-based MOF was 96.2 μmol h^{-1} mmol MOF^{-1} and this was higher than conventional Zr-based MOF without any conjugated functional group such as amine. It was suggested from experimental results that organic ligand and LMCT process to Zr_6 oxocluster were reasons for demonstrating higher photoreduction ability [84].

Instead of amino group, Zhongmin et al. utilized and conjugated visible-light response type organic ligand derived

from an anthracene group to synthesize zirconium-based MOFs. As this was also zirconium-based MOFs, prepared material demonstrated high thermal, chemical stability and CO_2 absorption ability. Anthracene group also was able to extend the light absorption to visible-light range and indicated high formate formation rate of 183.3 μmol h^{-1} mmol MOF.$^{-1}$. From the series of electron paramagnetic resonance (EPR), analysis and experimental results revealed that anthracene-based ligand and building unit Zr_6 oxo cluster were the origin for demonstrating high photocatalytic activity. [85]

As we have seen in Fe-based MOF section, incorporating foreign substance to MOF is one of other strategy to improve photocatalytic activity. Serre et al. had introduced copper nanoparticles into 2 typical zirconium-based MOFs: MOF-801 and UiO-66-NH_2. They also carried out room temperature scalable synthesis procedure for considering real industrial application [86]. Initially, copper (Cu) nanoparticle was synthesized with using L-ascorbic acid as reducing and capping agent. On the other hand, zirconium oxocluster was prepared from $ZrCl_4$ and then after, these 2 components were mixed to prepare final Cu–Zr-MOFs composite. With this procedure, the size of Cu–Zr-MOFs composite material became smaller as more quantity of Cu nanoparticle was added within the experimental synthesis condition (Fig. 9a). One could also observe Bragg peak broadening as concentration of Cu nanoparticle increases. This kind of phenomenon is often seen in a nucleation process-induced seed-mediated crystal growth, in which seeds of small Cu nanoparticles behave as nucleation sites and suppress further crystal growth. High-resolution transmission electron microscopy and particle size analysis elucidated that prepared Cu nanoparticles are well dispersed in the solution with the average size of 1.6 nm (Fig. 9b, c). Cu–Zr-MOF composite was yellowish color and plasmonic absorption peak which originates from quantum size effect did not appear much (Fig. 9e) [87, 88]. This type of prepared Cu–Zr-MOF composite presented more of core–shell structures rather than Cu being embedded in MOF pore (aperture of MOF 5–7 Å is much smaller than 1.6 nm). As a result, it indicated high CO_2 photoreduction rates of 94 μmol h^{-1}.

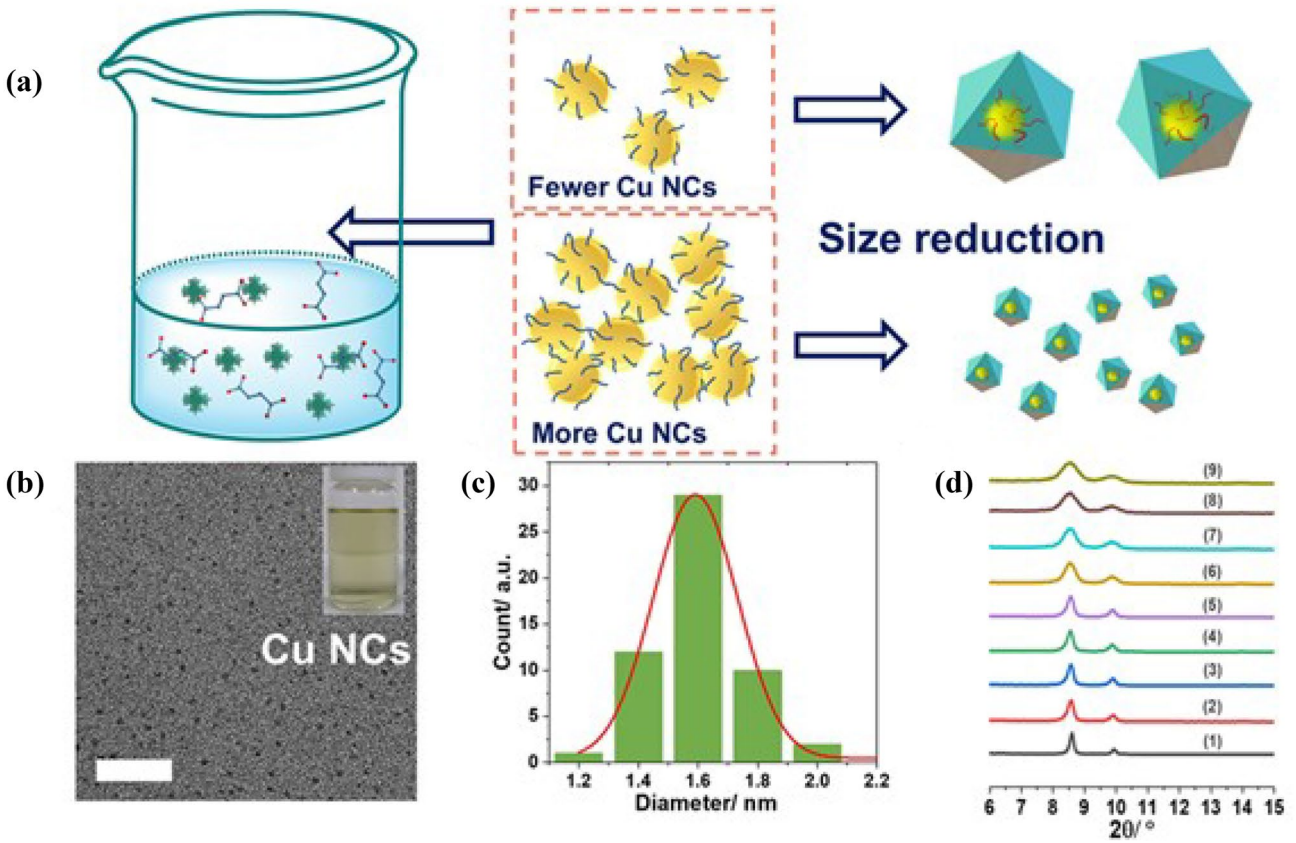

Fig. 9 **a** Representation of the Cu nanoparticles concentration-dependent size reduction of the prepared Cu nanoparticles/MOF-801. **b** TEM images of Cu nanoparticles. Insert: a photograph of the synthesized Cu nanoparticles. **c** particle size distribution of the synthesized Cu nanoparticles. **d** PXRD patterns (λCu = 1.5406 Å) of MOF801(1) and Cu nanoparticles/MOF-801 with increasing Cu nanoparticles loading from 64 to 6.4 mmol (labeled with 1–9)

In addition to metal particle, as we have seen in Fe-based MOF section, graphitic carbon nitride quantum dots (g-CNQDs) was introduced to zirconium-based MOF to prepare composite (g-CNQDs/MOF) as CO_2 photocatalytic reduction material [89]. Unique properties of g-CNQDs improved composite material catalytic activity by enhancing conductivity and extending the life time of photogenerated charge due to effective electron–hole pair separation. As a result, g-CNQDs/MOF composite converted CO_2 into methanol with the rate of 386 μmol h^{-1} g^{-1}, which is much higher than the reaction efficiency promoted with MOF without g-CNQDs (66 μmol h^{-1} g^{-1}). Saikia et al. had proposed mechanism of this composite as depicted in Fig. 10. g-CNQDs absorb illuminated light energy and charge separation proceeds as first step. Then after, separated electron transport to semiconductor (MOF) surface to form catalytic sites. Since the conduction band of MOF higher than that of g-CNQDs, electron transfer from conduction band of g-CNQDs to valence band of MOF proceeds which results in displaying typical Z-scheme mechanism. In this situation, CO_2 photocatalytic reduction rate to form methanol of g-CNQDs/MOF is higher than sole MOF (NH_2-UiO-66) as photocatalytic material. In addition, $–NH_2$ functional groups on MOF surface adsorb more CO_2 than bare MOF surface that also contribute to gaining stronger CO_2 photocatalytic reduction. Thus, the combination of quantum dots and NH_2-terephthalate ligands can confer photogenerated electrons to possess longer lifetime to enhance the reaction. On the other hand, holes generated by photoexcitation in the valence band of g-CNQDs obtain electrons from trimethylamine to complete the CO_2 photocatalytic reduction reaction flow.

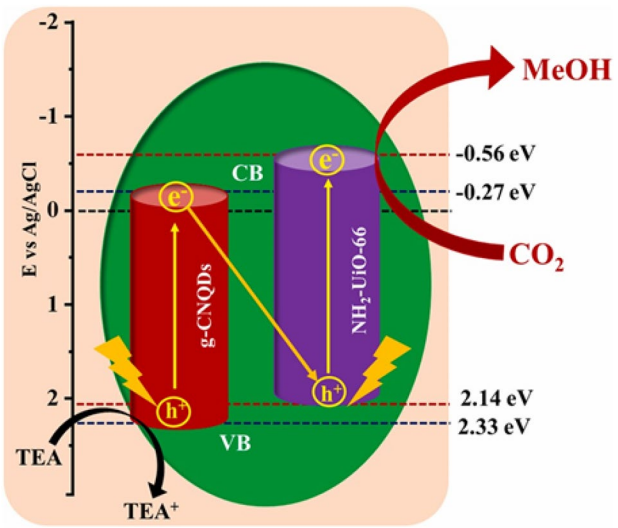

Fig. 10 Proposed mechanism of CO_2 reduction on composite as g-CNQDs/MOF

Besides foreign substance introduction to MOFs, defects in MOFs can confer more efficient charge separation and light absorption. Wang et al. prepared a few UiO-66-NH_2 with different types of defects to see the influence upon CO_2 photocatalytic reduction [90]. MOF with ligand vacant defect presented the strongest CO_2 photocatalytic reduction reaction compared to non-defect, missing cluster and monocarboxylate compensated ones indicated 9.2 times higher CO formation rate than missing cluster one. The relation between electronic properties such as E_{abs} (absorption energy) and E_{LMCT} (ligand-to-metal charge transfer energy), and photocatalytic activity in MOF defect structure was explained with DFT calculation. It was suggested that minimum energy total of E_{abs} and E_{LMCT} will decrease reaction energy barrier in the rate limiting step which can promote the CO_2 photocatalytic reduction.

It was possible to decrease the energy barrier to accelerate CO_2 photoreduction by applying appropriate doped metal to Zr-based MOFs. Conjugation of amine functional or anthracene group onto Zr-based MOFs also improved the catalytic reaction by promoting LMCT process to Zr_6 oxocluster as well as by enhanced light absorption. Introduction of foreign additive such as copper nanoparticles and quantum dot was also effective way to increase photocatalytic activity by obtaining higher conductivity and by extending the life time of photogenerated charge and following effective electron–hole pair separation by Z-scheme mechanism. Defect structure in MOF and amine functional group introduction also enhanced the photocatalytic reaction by increasing photoabsorption ability and by lowering the energy barrier, respectively.

Ti-based MOF for CO_2 photocatalytic reduction

In case of Ti-based MOF, MIL-125(Ti) ($Ti_8O_8(OH)_4(O_2CC_6H_4–CO_2)_6$) is the most investigated MOF, and that is composed of the $Ti_8O_8(OH)_4$ secondary building units (SBUs) and 1,4-benzenediacarboxylate (BDC) ligands. In addition, this type of MOF has been applied as photocatalytic materials. For example, CO_2 photocatalytic reduction with MIL-125(Ti) was carried out and 2.41 mmol of formic acid was generated in the acetonitrile (MeCN) solvent with TEOA as a sacrificial agent with 365 nm UV light irradiation for 10 h [91]. As in the case for Fe and Zr-based MOFs, various kinds of challenge have been performed upon Ti-based MOF, to strengthen photocatalytic activity including foreign substance or functional group introduction, metal doping and organic linker modification.

Zhang et al. prepared a few kinds of Cu_2^+-doped two-dimensional Ti-based MOFs with solvothermal synthesis procedure [92]. When the concentration of doped Cu_2^+ is

optimized, production rate of CH_4 was 3.7 μmol g^{-1} h^{-1} with 93% electron selectivity. Investigation of CO_2 adsorption, charge separation process, electronic and band structure revealed when the amount of doped Cu_2^+ is appropriately suitable to Ti-based MOF, thermodynamically confer the MOF conduction band position to have strong reduction potential for the photocatalytic reduction. In addition, photoexcited charge career generation, separation and transportation process was facilitated by controlling the local electronic circumstances around titanium oxide clusters.

Apart from metal doping to MOF, regulating facet of MOF crystalline is another strategy to influence the catalytic activity. Sun et al. had prepared NH_2-MIL-125(Ti) with different ratio of {001} and {111} facets by modifying the amount of DMF, methanol as solvent and acetic acid as catalyst, in the solvothermal synthesis [93]. In addition, it was found that the titanium tetraisopropanolate or titanium butoxide as titanium precursor also influenced the facet. The {111} facets indicated stronger CO_2 photocatalytic activity to convert to CO and CH_4 with yields of 8.25 and 1.01 mol g^{-1} h^{-1}, those are 9 and 5 times superior than yields of {001} facets, respectively. Figure 11a presents UV–visible-light absorption of prepared samples. 2 main absorption broad peaks around 300 and 400 nm correlate to the absorption of Ti−O_x clusters and organic ligand, respectively [94]. The absorption wavelength was red shifted as {111} facets ratio increased. Figure 11b displays the Tauc plots and from which highest occupied molecular orbital (HOMO) and lowest unoccupied molecular orbital (LUMO) gap can be figured out. Then, HOMO−LUMO gap

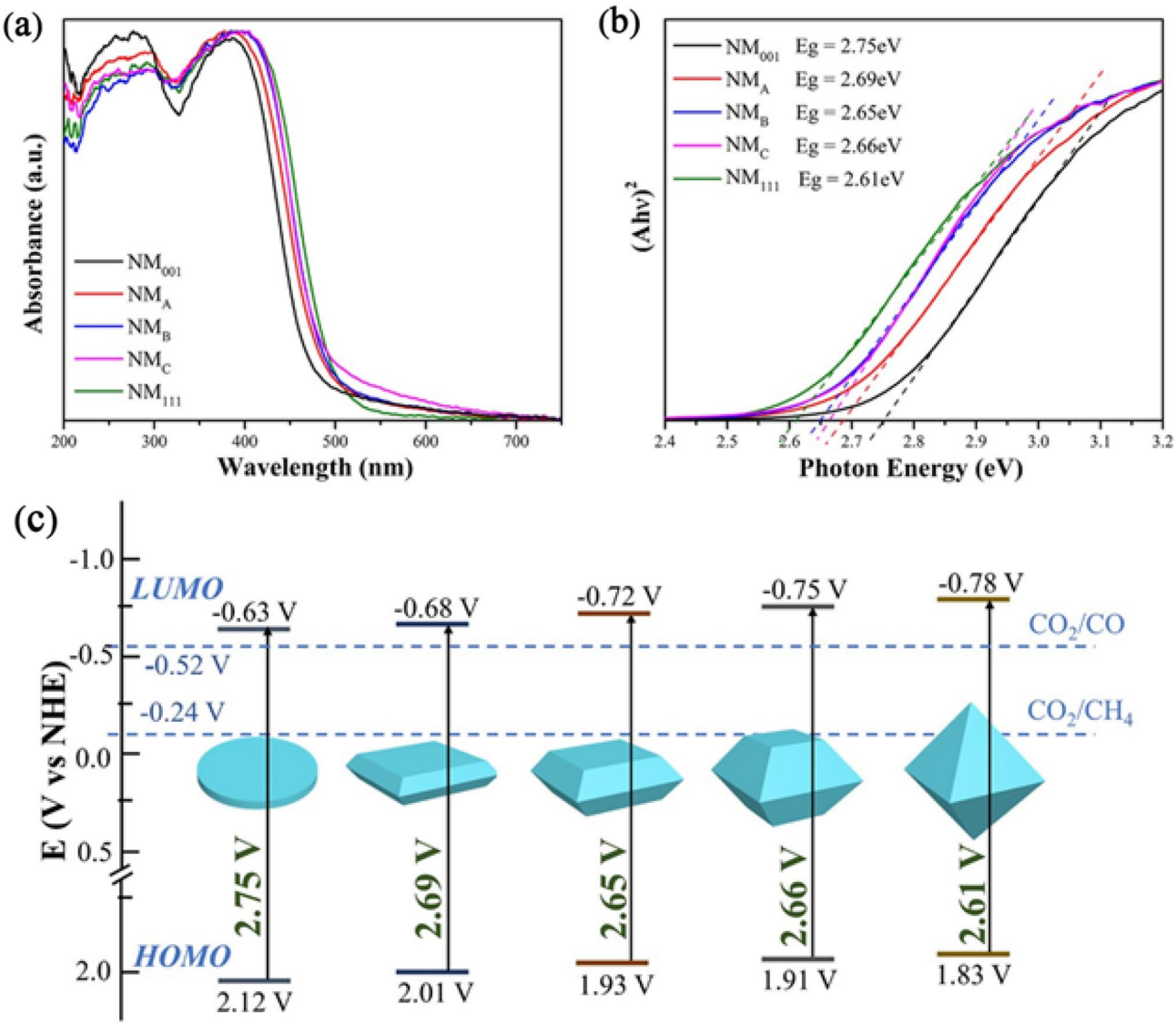

Fig. 11 **a** UV – Vis diffuse reflectance spectra, **b** Tauc plots, **c** HOMO−LUMO gap of the as-synthesized photocatalyst materials

can be considered as bandgap energy for MOFs as being semiconductor. Combined with the flat-band potential results obtained from Mott−Schottky plots, the calculated HOMO–LUMO bandgaps energies were 2.75 eV (NM001), 2.69 eV (NMA), 2.65 eV (NMB), 2.66 eV (NMC), and 2.61 eV (NM111) (Fig. 11c). It should be mentioned here that N represents as NH_2, M indicates as Mil-125 (Ti). In addition, facet is the number following 001 and 111, whereas A, B, C means mixed facet of 001 and 111 and C has the highest 111 facet. Thus, {111} facets in NH_2-MIL-125(Ti) is most promising face due to lowest bandgap energy, which means it only requires less solar energy. They also discovered that recombination rate of photoexcited electrons and holes are suppressed more on {111} facets. It was also found that the Ti (III) is the strong reducing agent for CO_2.

MOF was combined with carbonaceous material to create composite material with stronger catalytic activity. Bu et al. synthesized reduced graphene oxide and NH_2-MIL-125(Ti) composite material (rGO/NH_2-MIL-125(Ti)) by solvothermal procedure [95]. Prepared composite material generated mainly methyl formate of 1116 $\mu molg^{-1}\ h^{-1}$, which is more than twice of MOF without graphene oxide. It was suggested that introduction of reduced graphene oxide and amino functional group to MOF was effective to enhance CO_2 photocatalytic activity. They had inferred that uniformly dispersed catalytic material also accelerated the effective photoexcited carrier separation and transfer. SEM observation of MIL-125(Ti), NH_2-MIL-125(Ti) and the composite rGO/NH_2-MIL-125(Ti) are displayed in Fig. 12. MIL-125(Ti) exhibited smooth surface with tablet like form with approximate size of 1 µm, and when amino group was conjugated, much smaller MOF particles were obtained. However, the dispersion status became worse by aggregation compared to the one without amino group. When rGO was introduced, uniformly dispersed MOF distribution had recovered by easing the aggregation probably due to layered structure of reduced graphene oxide.

Modifying the organic linker for Ti-based MOF is another way to obtain alternative MOF instead of MIL-125(Ti). Wang et al. introduced isophthalic acid (IPA) as organic linker instead of 1,4-benzenediacarboxylate (BDC) ligands for MIL-125(Ti). By changing the dicarboxylic groups positioning from para to meta-position on benzene ring, they have successfully synthesized Ti-IPA MOF (MIP-208) [96]. They had also clarified that the prepared MOF exhibited robust water resistance. MIP-208 was soaked in water at room temperature and boiling water. XRD patterns indicate that those samples were identical to as prepared samples prove high water stability of this type of MOF material (Fig. 13a). Furthermore, CO_2 adsorption ability did not get influenced by even boiling water treatment as shown in Fig. 13b. It should be noted here that MIP-208 was stable even under aqueous solution with various pH values ranging from strong acid to base condition. Ruthenium oxide nanoparticles were combined to MIP-208 in order to obtain strong catalytic material and demonstrated excellent visible-light response type CO_2 methanation photoactivity.

Metal complex was incorporated to MOF as foreign substances to enhance its activity. Zn(II)-porphyrin was coordinated with titanium oxoclusters as photosensitizer to provide NH_2-MIL-125(Ti) with higher CO_2 adsorption capability and photocurrent [97]. 11 times higher photocatalytic activity was achieved to convert CO_2 to CO. Since 1,4-benzenediacarboxylate (BDC) ligands was used to build

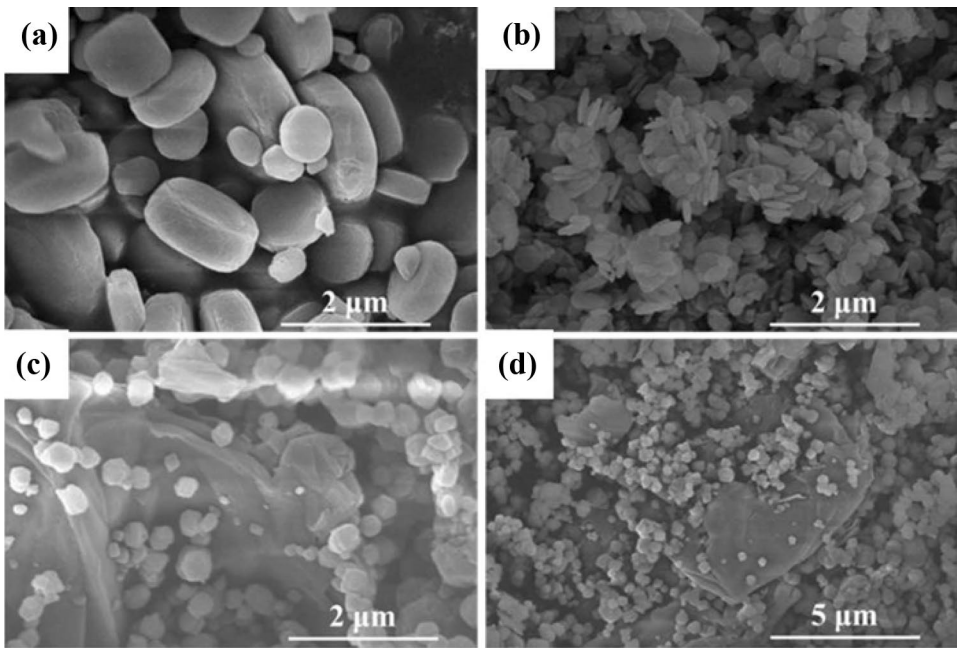

Fig. 12 SEM images of MIL-125 (**A**), NH2-MIL-125 (**B**), rGO@NH2-MIL-125 (**C**, **D**)

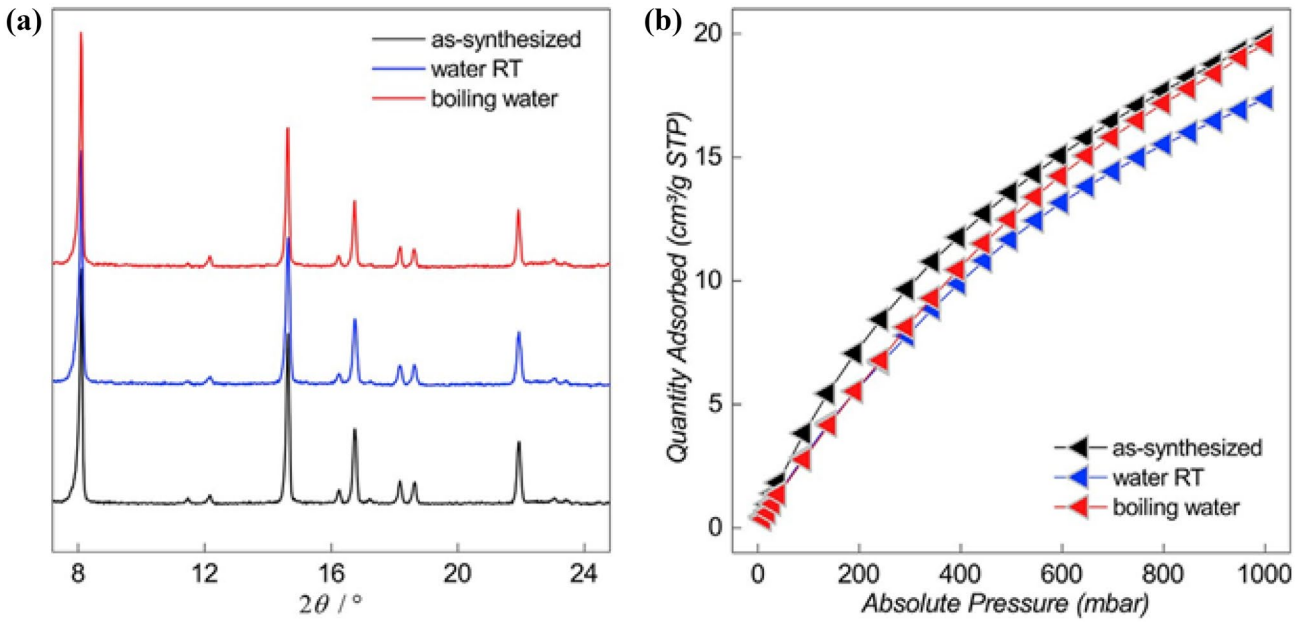

Fig. 13 **A** PXRD patterns for the MIP-208 samples before and after water treatments. **B** CO_2 adsorption isotherms collected at 298 K for the MIP-208 samples before and after water treatments

MOF structure already and porphyrin was applied as second ligand, Li et al. refer this type material as dual-ligand Ti-based MOFs and suggest MOF prepared by porphyrin-metal oxoclusters coordination is one of the alternative way to enhance CO_2 photocatalytic reduction reaction.

MOF-based photocatalytic material can be not only powder, but different material form. Aerogel type MOFs were obtained by reacting Ti(IV) oxo-clusters and aromatic dicarboxylic linkers and following supercritical drying procedure [98]. Prepared aerogels were composed of approximately 5–10 nm sized nanoparticles linked microstructure with surface area being smaller than its counterparts MOFs. Even though, CO_2 photocatalytic reduction reaction was higher due to more fluent diffusion of reagent and chemical reaction. This is because intrinsic MOF pore size and structure in the powder form are too small for smooth chemical reaction. So that a little larger pore and structure of this aerogel type MOF promoted the CO_2 photocatalytic reduction more efficiently.

MIL-125(Ti) are the representative Ti-based MOFs. Introduction of foreign additive such as copper nanoparticles enhanced the CO_2 photoreduction activity by tuning the conduction band position to have strong reduction potential, as well as accelerating photoexcited charge career generation, separation and transportation process by optimizing the local electronic environment around titanium oxide clusters. MOF crystalline facet regulation was effective to enhance photocatalytic activity by decreasing bandgap energy and suppressing the photogenerated electron–hole pair recombination rate. Introduction of carbonaceous material such as reduced graphene oxide to MOF was also an effective way, by tuning the morphology of catalytic materials. It was also found that the stability of MIL-125(Ti) was strengthened by replacing 1,4-benzenediacarboxylate (BDC) to isophthalic acid (IPA) as organic linker.

Ti–Zr-based MOF for CO_2 photocatalytic reduction

Partial substitution of metal cations in MOFs can introduce metal-to-metal charge transfer, which can promote photocatalytic performance especially under visible-light irradiation [99]. When one considers about electrochemical potential, Zr-based MOF has more negative redox potential than Ti-based MOF (Ti_4^+/Ti_3^+ (− 0.1 V), Zr_4^+/Zr_3^+ (− 1.06 V)) [100]. Even though, UiO-66 indicates no response with visible light because LUMO of 1,4-benzenediacarboxylate (BDC) ligands is lower than $Zr_6O4(OH)_4$ redox potential energy level in UiO-66. This fact results in low efficiency in LMCT and consequently low rate reaction in CO_2 photocatalytic reduction. In this respect, a bimetallic UiO-based MOF, NH_2-UiO-66(Zr/Ti), was synthesized by Cohen by partially replacing Zr in NH_2-UiO-66(Zr) with Ti [101]. The bimetallic MOF as NH_2-UiO-66(Zr/Ti) demonstrated stronger CO_2 photocatalytic activity than NH_2-UiO-66 (Zr) upon visible-light irradiation. This is due to Ti ion introduction, MOF can accept photoexcited electrons from organic linkers by light absorption. Since they could not detect formic acid

formation with sole UiO-66(Zr)-NH_2, it is clear that Ti addition was critical factor.

Two types of NH_2-UiO-66(Zr/Ti) MOFs with different Zr and Ti molar ratio (Zr: Ti = 120:16, 100:4) were synthesized compared CO_2 photocatalytic performance under visible light [102]. Both Ti introduced Zr-based MOF exhibited stronger photoactivity than sole Zr-based MOF although NH_2-UiO-66(Zr/Ti) MOF (Zr:Ti = 120:16) indicated even stronger activity than the other one. It was found that photocatalytic and CO_2 adsorption sites were augmented by Ti addition which contributed upon higher photocatalytic activity. Speculated scheme for enhanced activity is depicted in Fig. 14b. When Ti_4^+ in added to $Zr_6O_4(OH)_4$ to replace with Zr_4 + center, the visible light-generated electrons in NH_2-BDC prefers to be transport to Ti_4^+ rather than Zr_4^+ which would result in forming $(Ti_3^+/Zr_4^+)_6O_4(OH)_4$ SBUs. This preference was theoretically calculated result. And this Ti_3^+ behave as electron donor to give away electrons to Zr_4^+ and thus, Zr_4^+ become Zr_3^+ to structure Ti_4^+–O–Zr_3^+ formation. As such, introduced Ti promotes charge transfer from the excited NH_2-BDC to Zr–O clusters, leading to enhancing the CO_2 photocatalytic reduction process.

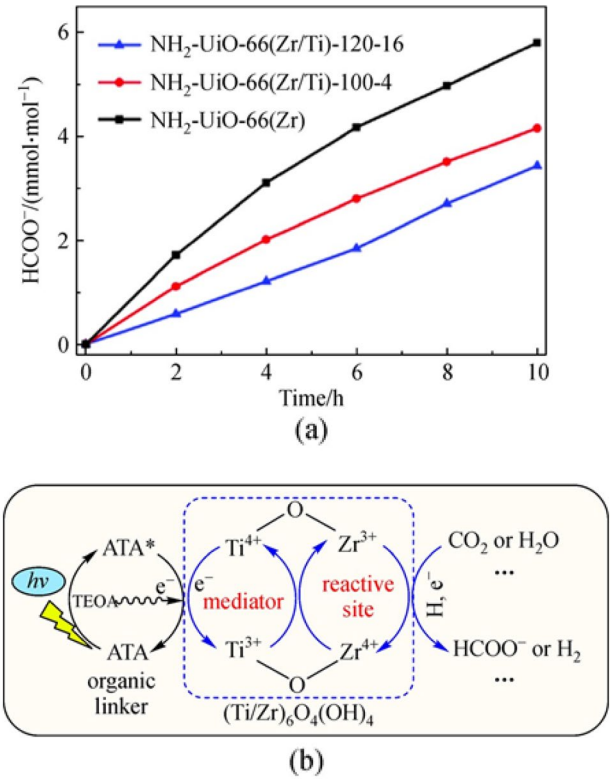

Fig. 14 HCOO amount formed with different samples as a function of light irradiation time. Improved CO_2 photocatalytic reduction of Ti addition to NH_2-UiO-66(Zr) and the proposed CO_2 mechanism

Syzgantseva et al. also studied the metal doping (substituting) effect to MOFs. Doped metal in a MOF would influence host electronic energy levels (Fig. 15) [99]. Therefore, it is important to refer the energy level of introducing metal kind as well as its electron affinity to optimize the whole energy diagram for the purpose. A metal with high electron affinity will often place energy state in the conduction band below the ligand level. The magnitude of electron level regulation degree would depend upon the doped metal content so that concentration of metal additive needs to be carefully controlled.

These are typical examples to demonstrate MOF characteristic improvement by adding or partially replacing metal to original MOF metal center in which can contribute enhancing photocatalytic CO_2 reduction. This phenomenon can be explained by photoexcited electrons transfer preference towards replaced metal.

Al-based MOF for CO_2 photocatalytic reduction

Robatjazi et al. had approached to prepare composite material in the interesting way based on Al-based MOF. They grew MIL-53(Al) shell layers surrounding on aluminum nanocrystals and this composite material exhibited photocatalytic activity with enhanced plasmonic effect. The MOF

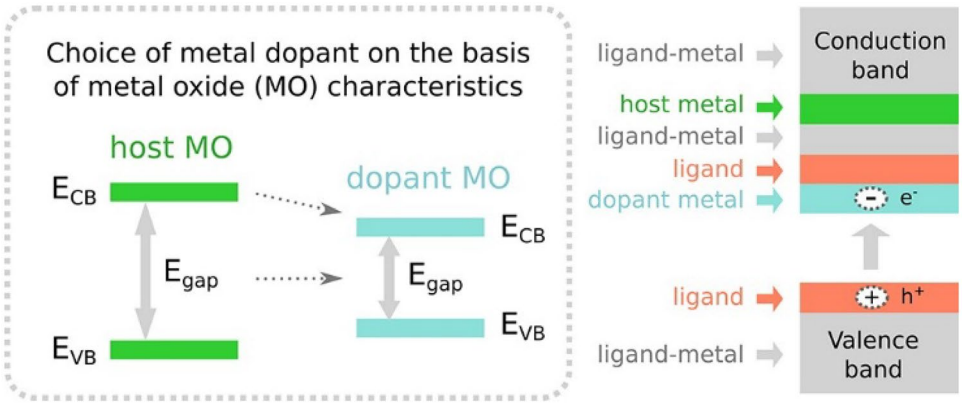

Fig. 15 Regulation of bandgap, conduction band alignment, and creation of localized electron traps applying metal doping to a MOF

synthesis on Al nanoparticle surface proceeded as dissolution of aluminum oxide layer on the nanoparticle surface to obtain Al^{3+} ions which was consumed for MIL-53(Al) growth. In other words, the dissolution of the Al nanoparticle surface oxide (Al_2O_3) layer served as a source of Al^{3+} for the backbone of the MOF (MIL-53(Al)) and promoted its growth so that it was unnecessary to introduce an additional aluminum metal precursor. 1,4-Benzenedicarboxylic acid (H_2BDC), which is the organic linker of MIL-53(Al), was selected as linker parts. It should be noted here that this (MIL-53(Al)) is of particular interest because of its excellent thermal and chemical stability, which could be good advantage for real practical usage [103]. In addition, plasmonic metal nanoparticles have gained significant attention for photocatalytic reaction due to their capability to activate chemical transformations on their surfaces under illumination. The plasmon resonant interaction with light upon metallic nanoparticles results in the generation of energetic hot carriers upon plasmon decay. There are some studies stating that plasmonic nanoparticles are able to enhance the photocatalytic performance by light scattering, light concentration, hot electron injections, and plasmon-induced resonance energy transfer. So far, most of this plasmon research was carried out with gold and silver nanoparticles to enhance photocatalytic activities. In contrast, recently, aluminum nanoparticles as in this case have been demonstrated as an earth-abundant, low-cost alternative to Au an Ag for plasmon-mediated photocatalysis, which is beneficial to real industrial application [104].

Salguero et al. synthesized a heterogeneous photosensitizer composite Ru@dpdhpzBASF-A520 by incorporating surface dipyridyl-dihydropyridazine additive by Diels–Alder reaction on the aluminum fumarate units of the highly porous metal–organic framework (MOF). They have furthermore modified with ruthenium metal to obtain final catalyst material. The light absorption characteristic in the visible-light region elucidated that prepared material can behave as a photocatalytic catalyst for hydrogen evolution together with Pt nanoparticles. EDTA as sacrificial electron donor and MV (methyl viologen) as electron carrier. High photocatalytic activity was observed even after 72 h of reaction indicating effective stabilization of the ruthenium dipyridyl-dihydropyridazine adducts on the MOF surface. Aluminum-based MOF was synthesized with aqueous solution of $Al_2(SO_4)_3{\cdot}18H_2O$ and fumaric acid together with NaOH as synthesis catalyst. This is the photocatalytic reduction reaction of proton in water and not CO_2 although confers an idea as utilizing this type of MOF composite material [105].

Musyoka et al. prepared Cu–ZnO catalysts supported on an aluminum fumarate metal–organic framework (Al Fum MOF) and applied as effective catalyst material for converting CO_2 to valuable chemical products. To make Al Fum MOF, solvothermal synthesis was carried out with $AlCl_3{\cdot}6H_2O$ and fumaric acid as precursors. Cu and ZnO were deposited on MOF by adding aqueous solution of $Cu(NO_3)_2.3H_2O$ and $Zn(NO_3)_2{\cdot}6H_2O$ and following 350 °C heat treatment in Argon. The catalysts were denoted as the theoretical weight percent composition of 7/3/90 (7Cu/3ZnO/AlFum MOF) and 15/6.4/78.6 (15Cu/6.4ZnO/AlFum MOF), respectively. The CO_2 conversion test results were presented in Fig. 16 including a commercial catalyst which is composed of Cu/Zn/Al/Mg. The one of the direct CO_2 hydrogenation to methanol reaction can be expressed as the equation: $CO_2 + 3H_2 \leftrightarrow CH_3OH + H_2O$. In addition to methanol, the reaction produced CO ($CO_2 + H_2 \leftrightarrow CO + H_2O$), H_2O, and CH_4 ($CO_2 + 4H_2 \leftrightarrow CH_4 + 2H_2O$). The 15Cu/6.4ZnO/AlFum MOF catalyst had the strongest CO_2 conversion in comparison to the commercial catalyst and the 7Cu/3ZnO/AlFum MOF catalyst. Furthermore, the prepared MOF-based catalyst exhibited good stability over the 24 h testing period [106].

Similar challenges are being attempted to enhance CO_2 photocatalytic activity for Al-based MOFs such as addition of metal nanoparticles and metal complex. Furthermore, it was shown that metal nanoparticles to demonstrate plasmon effect such as Ag, Au, Pt as well as Al nanoparticles could enhance catalytic activity by light scattering, light concentration, hot electron injections, and plasmon-induced resonance energy transfer.

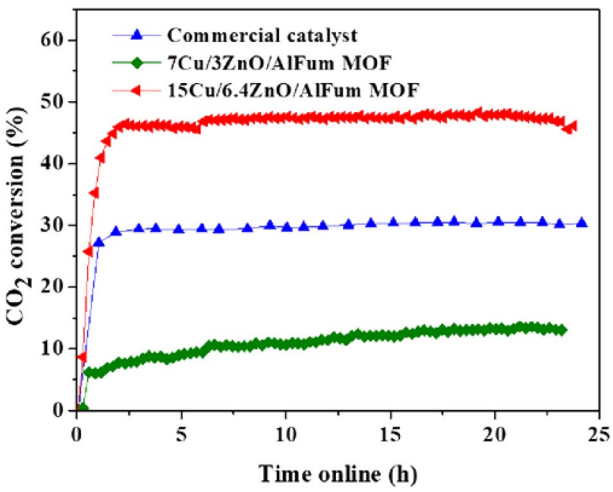

Fig. 16 CO_2 conversions of the evaluated catalysts. Temperature = 230 °C; pressure = 50 bar; Qv, 0 = 40 mL min^{-1}; gas hourly space velocity = 10,000 h − 1; $H_2/CO_2 = 3:1$

Organic linkers influence upon CO_2 photoreduction activity

Besides discussing about metal center in MOF-based catalytic materials, it is known that organic linker, ligands also largely influence the photocatalytic activity of MOF-based catalysts [71]. Some example of amino functional group conjugated MOF were introduced in this study although in terms of stability and robustness, aromatic organic linkers would be more ideal since they can provide structural rigidity and hydrophobicity towards MOF than the aliphatic linkers do. When this aromatic ligand is properly selected, it would offer an additional advantage to obtain higher photolytic activity. For example, hydrophobic MOF (MIL-125-NHCyp, Cyp = cyclopentyl) were prepared for CO_2 photoreduction reaction especially in humid environment owing to its stability against water. MIL-125(Ti) with three functional groups has been synthesized with $–NH_2$, –NHMe, and –NHCyp as organic linker moiety, respectively. Among these 3 MOFs, MIL-125-NHCyp demonstrated the strongest stability and CO_2 photoreduction activity due to its hydrophobic nature and the steric blocking effect of cyclopentyl group towards hydrogen bond and water [107].

Even amine functionalization of MOFs do not obviously possess strong hydrophobicity as aromatic linker, they exhibited higher CO_2 adsorption capacity as well as reduction capability owing to their porous topological texture and appropriate binding energy reduction reaction. MIL-101 (Cr) was grafted with different type of alkylamine such as ethylenediamine (EN), diethylenetriamine (DETA), and triethylenetetramine (TETA). It was clarified that MIL-101 (Cr) EN demonstrated the best photoactivity and extended efficient electron transfer with suppressed charge recombination. It was also found that surface area was decreased due to clogging of MOF pores by DETA and TETA which was speculated to be the lower efficiency for their cases [68].

The polyoxometalate (POM: TBA5[$P_2Mo_{16}{}^{V}Mo_8{}^{VI}O_{71}(OH)_9Zn_8(L)_4$])-based MOF was in situ synthesized and demonstrated high hydrophobicity due to its ligand structure which also exhibited efficient photocatalytic CO_2 reduction performance. Formic acid was produced with the yield of 35.2 µmol in the aqueous solution with 97.9% of selectivity [108].

Furthermore, as we described in this study, porphyrin is often applied as foreign material to combine with MOF in order to extend MOF light response to visible-light range owing to their aromatic structure. Porphyrin-based zirconium MOFs (PCN-H_2/Pt) with H_2TCPP and Pt^{II}TCPP [TCPP = tetrakis(4-carboxyphenyl)porphyrinate] as isostructural ligands and Zr_6 clusters as metal nodes was prepared. PCN-H_2/Pt exhibited high H_2 production rate of 351.08 µmol h^{-1} g^{-1} even under visible-light irradiation. This is due to evenly distributed Pt^{2+} ions in PCN-H_2/Pt, which accelerate the charge transfer from porphyrins to Pt^{II} ions, which resulted in efficient charge separation in the MOF composite materials [109].

As we described above, various attempts have been challenged in order to enhance the efficiency of CO_2 photoreduction to convert them into various chemicals such as CO, CH_3OH, H_2, and CH_4. Despite a numerous number of challenged have being made such as optimizing the metal center and ligand, there are still many challenges in achieving MOF-based artificial photosynthesis in practical applications.

Table 3 summarize the MOF-based CO_2 photoreduction system presented in this study. As it was discussed in this article, most of their challenges are trying to confer ability to MOF-based photocatalytic materials, to work under not only ultraviolet light but also visible light. Suppressing the recombination of photoexcited electron–hole pairs and expanding lifetimes of charge carriers is also an important issue. In addition, it should be necessary not to utilize sacrificial reagents such as TEOA because that would be obvious extra cost for artificial photosynthesis system for real industrial application.

It should be mentioned here that when one considers about real industrial application for MOF-based CO_2 photoreduction system, MOF synthesis as well as mass manufacturing process is extremely important since MOFs synthesis are time consuming in general.

Table 4 summarized the representative MOF synthesis procedure so far in the past research and also explain some merits and demerits at each method [110, 111]. From author's group experience that mechanochemical synthesis seems most plausible method for real industrial application although they suffer from low crystallinity and decreased pore volume and surface area.

Raja et al. also explained the influence upon photocatalytic activity of MOF, of metal additive including Pt, Au, Ag and Rh noble metals as well as Co, Ni, Fe and Cu as non-noble conventional metal as considered for real industrial application. They have also investigated the impact of miscellaneous species such as reduced graphene oxide, g-C_3N_4 and carbon dots. Besides photocatalytic activity upon illuminated light wavelength, they claim that the size of MOF crystallites, surface area, length of organic linker, location of foreign additive, oxidation state as well as unsaturated metal center site in MOFs also have impact on catalytic activities [112]. For example, in general, MOF with smaller size and large surface area would possess higher photocatalytic activity due to increased reaction area.

It should be noted here that author's group have recently found one interesting efficient mechano-chemical process

Table 3 Summary of photoreduction reaction of CO_2 with MOFs and MOFs composite materials presented in this study

Photocatalyst	Active metal cluster	Organic metal linker	Photocatalytic reaction condition				Throughput (μmol/g)					Refs.
			Solvent	Power	Sacrificial agent	Irradition Time	CO	CH_4	H_2	$HCOO^-$	CH3OH	
MIL-100(Fe), MIL-101(Fe)-NH_2, MIL-88B(Fe), MIL-88B(Fe)-NH_2	Fe–O											[72]
MIL-100(Fe), MIL-101(Fe)	Fe–O											[73]
MIL-101(Fe), MIL-53(Fe), MIL-88B(Fe)	Fe–O				TEOA							[74]
Fe-Al-SBA-15 (SBA:silica)	Fe–O											[75]
NH2-MIL-101(Fe)	Fe–O											[76]
NH2-MIL-53(Fe), NH2-MIL-88B(Fe), NH2-MIL-101(Fe)	Fe–O	H_4L	Solvent-Free	300-W xenon arc lamp ($400 < \lambda < 800$)	TEOA	5 h	87.6					[52]
MAPbI3 QD @ PCN-221	Fe–O	TCPP	Ethyl acetate/water	300 W Xe-lamp	H_2O	80 h	1559	325				[80]
Co-UiO-67 and Re-UiO-67	Zr-O											[83]
Zr-SDCA-NH2	Zr-O	H2SDCA								96.2		[84]
	Zr-O	NNU-28								183.3		[85]
Cu NCs@MOF-801 and Cu NCs@UiO-66-NH2	Zr-O	BDC								95		[86]
AuNR@Zr-MOF	Zr-O	NU 901										[87]
g-CNQDs@NH2-UiO-66	Zr-O	BDC									386	[89]
UiO-66-NH_2	Zr-O	BDC										[90]
NH2-MIL-125(Ti)	Ti–O	BDC	MeCN	365 nm UV light irradiation	TEOA	10 h						[91]
Cu doped Ti-MOF	Ti–O				H_2O		1.2	3.7				[92]
NH2-MIL-125(Ti)	Ti–O	BDC					8.25	1.01				[93]
g-C3N4/CuO@MIL-125(Ti)	Ti–O	BDC			H_2O		180.1				997.2	[94]
rGO / NH2-MIL-125(Ti)	Ti–O	BDC								1116	[	[95]
MIP-208@RuOx	Ti–O	Isophthalic acid										[96]
MIL-125-NH2	Ti–O	BDC	$KHCO_3$ in Water	450 nm LED	H_2O						786	[98]

Table 3 (continued)

Photocatalyst	Active metal cluster	Organic metal linker	Photocatalytic reaction condition				Throughput (μmol/g)					Refs.
			Solvent	Power	Sacrificial agent	Irradition Time	CO	CH_4	H_2	$HCOO^-$	CH3OH	
MIL-125, UiO-66	Ti–O, Zr-O	BDC										[101]
Ru@dpdhpzBASF-A520	Al-O	Fumaric acid	Acetate	Visible light (450 nm)	TEOA				26			[105]
Cu/Zn on AlFum MOF,	Al-O	Fumaric acid										[106]

Table 4 Summary of MOF synthesis procedure and each merits and demerits

Solvothermal method	Merits	One step synthesis
		Single crystallinity
		Moderate temperature
	Demerits	Long reaction time
		Require more solvents
		By-products production
Mechano chemical	Merits	Ambient temperature
		Less by-products
		Lses time consuming
		Environmentally friendly
	Demerits	Low crystallinity
		Lower pore volume and surface area
Microwave assisted	Merits	Uniform morphology
		Rapid synthesis
		High purity
	Demerits	Difficult for l industrial procedure
		Difficult to obtain single crystalline
Electrochemical	Merits	Mild reaction condition
		Metal salts are unnecessary
		Less time consuming
	Demerits	Low production yield
		N_2 atmosphere is necessary
		Varied structure
Sono chemical	Merits	Fast and environmentally friendly
		Homogeneously nucleation
		Room temperature synthesis
		Modulate crystallization time
	Demerits	Difficult to obtain single crystalline

for MOF production and also developed zirconium-based MOF/carbon quantum dot composite and applied for CO_2 photocatalytic reduction to generate formic acid. The detail mechanism of this reaction will be coming in a forthcoming paper.

Conclusion

To apply MOF as CO_2 photocatalytic reduction process, we chose Fe, Zr, Ti and Al as metal center for MOFs catalyst for CO_2 photocatalytic reduction materials. This is because these 4 metal doped MOFs are relatively abundant materials and economically friendly compared to other precious rare earth or earth metals. It was demonstrated that the intrinsic bandgap energy depends on the metal center, which should be suitable for CO_2 photocatalytic reduction. For example, when Fe is the MOF metal center, Fe_3O cluster can be the

origin for visible-light irradiation. CO_2 adsorption capacity as well as photoreduction reaction also can be augmented by selecting or doping with appropriate metal. Functionalization of MOF with organic substances such as amine group to organic linker accelerate the electron transfer by ligand-to-metal charge transfer (LMCT) reaction and increase CO_2 absorption as well as light absorption extension to visible-light range, which eventually enhanced the CO_2 photocatalytic reduction. Metal nanoparticles introduction to MOF enhanced the CO_2 photoreduction by tuning the conduction band position, accelerating photoexcited charge career generation, separation and transportation process, as well as their plasmon effect. Quantum dot-MOF composite materials demonstrated higher CO_2 photocatalytic activity by enhancing quantum dot durability, extension of light absorption to visible-light range and fast charge transfer to metal center catalytic site of MOF. In addition, MOF crystalline facet regulation was effective to enhance photocatalytic activity by decreasing bandgap energy and suppressing the photogenerated electron–hole pair recombination rate.

Acknowledgements The author wishes to express thanks to Mr. Hirohisa Iwabayashi and Dr. Hideki Yoshioka for their helpful discussions.

Data availability The authors declare that the data supporting the findings of this study are available within the paper.

Declarations

Conflict of interest There are no conflicts to declare.

Consent for publication The author declares that the work submitted for publication indicated above is original, has not been published before, and is not under consideration for publication anywhere. This statement and declaration have been approved by all the co-authors.

References

1. Lingampalli, S.R., Ayyub, M.M., Rao, C.N.R.: Recent progress in the photocatalytic reduction of carbon dioxide. ACS Omega **2**, 2740–2748 (2017)
2. Xia, Y.S., et al.: Tandem utilization of CO_2 photoreduction products for the carbonylation of aryl iodides. Nat. Commun. **13**, 2964–2975 (2022)
3. Wang, B., Chen, W., Song, Y., Li, G., Wei, W., Fang, J., Sun, Y.: Recent progress in the photocatalytic reduction of aqueous carbon dioxide. Catal. Today **311**, 23–39 (2018)
4. North, M., Pasquale, R., Young, C.: Synthesis of cyclic carbonates from epoxides and CO_2. Green Chem. **12**(9), 1514–1539 (2010)
5. Li, W., Wang, H., Jiang, X., Zhu, J., Liu, Z., Guo, X., Song, C.: A short review of recent advances in CO_2 hydrogenation to hydrocarbons over heterogeneous catalysts. RSC Adv. **8**(14), 7651–7669 (2018)
6. Raciti, D., Wang, C.: Recent advances in CO_2 reduction electrocatalysis on copper. ACS Energy Lett. **3**(7), 1545–1556 (2018)
7. Kovačič, Z., Likozar, B., Huš, M.: Photocatalytic CO_2 reduction: a review of ab initio mechanism, kinetics, and multiscale modeling simulations. ACS Catal. **10**(24), 14984–15007 (2020)
8. Ma, Y., et al.: Selective photocatalytic CO_2 reduction in aerobic environment by microporous Pd-porphyrin-based polymers coated hollow TiO_2. Nat. Commun. **13**, 1400–1409 (2022)
9. Zhang, L., Zhang, J.: Metal-organic frameworks for CO_2 photoreduction. Front. Energy **13**(2), 221–250 (2019)
10. Li, K., Peng, B., Peng, T.: Recent advances in heterogeneous photocatalytic CO_2 conversion to solar fuels. ACS Catal. **6**(11), 7485–7527 (2016)
11. Linsebigler, A.L., Lu, G., Yates, J.T.: Photocatalysis on TiO_2 surfaces: principles, mechanisms, and selected results. Chem. Rev. **95**(3), 735–758 (1995)
12. Tahir, M., Amin, N.S.: Advances in visible light responsive titanium oxide-based photocatalysts for CO_2 conversion to hydrocarbon fuels. Energy Convers. Manag. **76**, 194–214 (2013)
13. Matsubara, Y., Grills, D.C., Kuwahara, Y.: Thermodynamic aspects of electrocatalytic CO_2 reduction in acetonitrile and with an ionic liquid as solvent or electrolyte. ACS Catal. **5**(11), 6440–6452 (2015)
14. Meng, Y., Liu, G., Zuo, G., Meng, X., Wang, T., Ye, J.: A review on ZnS-based photocatalysts for CO_2 reduction in all-inorganic aqueous medium. Nanoscale **14**, 14455–14465 (2022)
15. Lu, Y., Guan, S., Hao, L., Yoshida, H., Nakada, S., Takisawa, T., Itoi, T.: Inactivation of SARS-CoV-2 and photocatalytic degradation by TiO_2 photocatalyst coatings. Sci. Rep. **12**, 16038–16045 (2022)
16. Ong, C.B., Ng, L.Y., Mohammad, A.W.: A review of ZnO nanoparticles as solar photocatalysts: synthesis, mechanisms and applications. Renew. Sustain. Energy Rev. **81**, 536–551 (2018)
17. Mishra, M., Chun, D.M.: α-Fe2O3 as a photocatalytic material: a review. Appl. Catal. A General. **498**, 126–141 (2015)
18. Bao, N., Shen, L., Takata, T., Domen, K.: Self-templated synthesis of nanoporous CdS nanostructures for highly efficient photocatalytic hydrogen production under visible light. Chem. Mater. **20**(1), 110–117 (2008)
19. Ahmaruzzaman, M., Mishra, S.R.: Photocatalytic performance of g-C3N4 based nanocomposites for effective degradation/removal of dyes from water and wastewater. Mater. Res. Bull. **143**, 111417 (2021)
20. Akter, J., Hanif, M.A., Islam, M.A., Sapkota, K.P., Hahn, J.R.: Selective growth of Ti_3^+/TiO_2/CNT and Ti_3^+/TiO_2/C nanocomposite for enhanced visible-light utilization to degrade organic pollutants by lowering TiO_2-bandgap. Sci. Rep. **11**, 9490–9501 (2021)
21. Meissner, D., Memming, R., Kastening, B.: Photoelectrochemistry of cadmium sulfide. 1. Reanalysis of photocorrosion and flat-band potential. J. Phys. Chem. **92**(12), 3476–3483 (1988)
22. Bahnemann, D.W., Kormann, C., Hoffmann, M.R.: Preparation and characterization of quantum size zinc oxide: a detailed spectroscopic study. J. Phys. Chem. **91**(14), 3789–3798 (1987)
23. Di, Z., Liu, C., Pang, J., Zou, S., Ji, Z., Hu, F., Chen, C., Yuan, D., Hong, M., Wu, M.A.: Metal–organic framework

with nonpolar pore surfaces for the one-step acquisition of C_2H_4 from a C_2H_4 and C_2H_6 mixture. Angew. Chem. Int. Edn. **134**(42), e202210343 (2022)
24. Li, S.L., Xu, Q.: Metal organic frameworks as platforms for clean energy. Energy Environ. Sci. **6**, 1656 (2013)
25. Gharagheizi, F., Yu, Z., Sholl, D.S.: Curated collection of more than 20,000 experimentally reported one-dimensional metal–organic frameworks. ACS Appl. Mater. Interfaces **14**(37), 42258–42266 (2022)
26. Sikma, R.E., Balto, K.P., Figueroa, J.S., Cohen, S.M.: Metal–organic frameworks with low-valent metal nodes. Ange. Chem. Inter. Edn. **61**(33), e202206353 (2022)
27. He, S., et al.: Metal–organic frameworks for advanced drug delivery. Acta Pharma. Sinica **11**(8), 2362–2395 (2021)
28. Hiraide, S., Sakanaka, Y., Kajiro, H., Kawaguchi, S., Miyahara, M.T., Tanaka, H.: High-throughput gas separation by flexible metal–organic frameworks with fast gating and thermal management capabilities. Nat. Commun. **11**, 3867–3881 (2020)
29. Sutton, A.L., Melag, L., Sadiq, M.M., Hill, M.R.: Capture, storage, and release of oxygen by metal–organic frameworks (MOFs). Ange. Chem. Inter. Edn. **61**(37), e202208305 (2022)
30. Yang, D., Gates, B.C.: Catalysis by metal–organic frameworks: perspective and suggestions for future research. ACS Catal. **9**(3), 1779–1798 (2019)
31. Yang, F., et al.: Applications of metal-organic frameworks in water treatment: a review. Small **18**(11), 2105715 (2021)
32. Lahcen, A.A., et al.: Metal organic frameworks meet molecularly imprinted polymers: insights and prospects for sensor applications. ACS Appl. Mater. Interfaces **14**(44), 49399–49424 (2022)
33. Wen, Y., Feng, M., Zhang, P., Zhou, H.C., Sharma, V.K., Ma, X.: Metal–organic frameworks (MOFs) as photocatalysts for the degradation of agricultural pollutants in water. ACS EST Eng. **1**(5), 804–826 (2021)
34. Zhao, R., Liang, Z., Zou, R., Xu, Q.: Metal–organic frameworks for batteries. Joule **2**(11), 2235–2259 (2018)
35. Das, I., Noori, M.T., Shaikh, M., Ghangrekar, M.M., Ananthakrishnan, R.: Synthesis and application of zirconium metal–organic framework in microbial fuel cells as a cost-effective oxygen reduction catalyst with competitive performance. ACS Appl. Energy Mater. **3**(4), 3512–3520 (2020)
36. Li, R., Zhang, W., Zhou, K.: Metal–organic-framework-based catalysts for photoreduction of CO_2. Adv. Mater. **30**(35), 1705512 (2018)
37. Zhang, W.D., et al.: High selectivity of photocatalytic reduction of CO_2 to CO based on terpyridine ligand supported CuI metal organic framework. Front. Chem. **10**, 1–11 (2022)
38. Maina, J.W., Pozo-Gonzalo, C., Kong, L., Schütz, J., Hill, M., Dumée, L.F.: Metal organic framework based catalysts for CO_2 conversion. Mater. Horiz. **4**(3), 345–361 (2017)
39. Zhang, T., Lin, W.: Metal–organic frameworks for artificial photosynthesis and photocatalysis. Chem. Soc. Rev. **43**(16), 5982–5993 (2014)
40. Horiuchi, Y., Toyao, T., Saito, M., Mochizuki, K., Iwata, M., Higashimura, H., Anpo, M., Matsuoka, M.: Visible-light-promoted photocatalytic hydrogen production by using an amino-functionalized Ti(IV) metal–organic framework. J. Phys. Chem. C **116**(39), 20848–20853 (2012)
41. Deria, P., Yu, J., Smith, T., Balaraman, R.P.: Ground-state versus excited-state interchromophoric interaction: topology dependent excimer contribution in metal–organic framework photophysics. J. Am. Chem. Soc. **139**, 5973–5983 (2017)
42. Wang, J.L., Wang, C., Lin, W.: Metal–organic frameworks for light harvesting and photocatalysis. ACS Catal. **2**(12), 2630–2640 (2012)
43. Jiang, D., Mallat, T., Krumeich, F., Baiker, A.: Copper-based metal organic framework for the facile ring-opening of epoxides. J. Catal. **257**(2), 390–395 (2008)
44. Wang, Q., Gao, Q., Enizi, A.M.A., Nafady, A., Ma, S.: Recent advances in MOF-based photocatalysis: environmental remediation under visible light. Inorg. Chem. Front. **7**, 300–339 (2020)
45. Cadiau, A., et al.: A titanium metal–organic framework with visible-light-responsive photocatalytic activity. Angew. Chem. Inter. Edn. **59**(32), 13468–13472 (2020)
46. Li, J., Chang, B., Zhao, H., Meng, Q., Li, M., Han, Q.: Visible-light-responsive polyoxometalate-based metal–organic framework for highly efficient photocatalytic oxidative coupling of amines. J. Mater. Sci. **56**, 6676–6688 (2021)
47. Chen, P., Guo, Z., Liu, X., Lv, H., Che, Y., Bai, R., Chia, Y., Xingm, H.: A visible-light-responsive metal–organic framework for highly efficient and selective photocatalytic oxidation of amines and reduction of nitroaromatics. J. Mater. Chem. A **7**, 27074–27080 (2019)
48. Chen, E.X., Qiu, M., Zhang, Y.F., Zhu, Y.S., Liu, L.Y., Sun, Y.Y., Bu, X.H., Zhang, J., Lin, Q.P.: Acid and base resistant zirconium polyphenolate–metalloporphyrin scaffolds for effcient CO_2 photoreduction. Adv. Mater. **30**, 1704388 (2018)
49. Qin, J.S., Yuan, S., Zhang, L., Li, B., Du, D.Y., Huang, N., Guan, W., Drake, H.F., Pang, J., Lan, Y.Q.: Creating well-defined hexabenzocoronene in zirconium metal–organic framework by post-synthetic annulation. J. Am. Chem. Soc. **141**, 2054–2060 (2019)
50. Wan, S., Ou, M., Zhong, Q., Wang, X.: Perovskite-type CsPbBr 3 quantum dots/UiO-66 (N_H2) nanojunction as efficient visible-light-driven photocatalyst for CO_2 reduction. Chem. Eng. J. **358**, 1287–1295 (2019)
51. Deng, X., Albero, J., Xu, L., García, H., Li, Z.: Construction of a stable Ru–Re hybrid system based on multifunctional MOF-253 for efficient photocatalytic CO_2 reduction. Inorg. Chem. **57**, 8276–8286 (2018)
52. Dao, X.Y., Guo, J.H., Wei, Y.P., Guo, F., Liu, Y., Sun, W.Y.: Solvent-free photoreduction of CO_2 to CO catalyzed by Fe-MOFs with superior selectivity. Inorg. Chem. **58**, 8517–8524 (2019)
53. Xu, H.Q., Hu, J., Wang, D., Li, Z., Zhang, Q., Luo, Y., Yu, S.H., Jiang, H.L.: Visible-light photoreduction of CO_2 in a metal–organic framework: boosting electron–hole separation via electron trap states. J. Am. Chem. Soc. **137**, 13440–13443 (2015)
54. Sun, D., Gao, Y., Fu, J., Zeng, X., Chen, Z., Li, Z.: Construction of a supported Ru complex on bifunctional MOF-253 for photocatalytic CO_2 reduction under visible light. Chem. Commun. **51**, 2645–2648 (2015)
55. Li, L., Zhang, S., Xu, L., Wang, J., Shi, L.X., Chen, Z.N., Hong, M., Luo, J.: Effective visible-light driven CO_2 photoreduction via a promising bifunctional iridium coordination polymer. Chem. Sci. **5**, 3808–3813 (2014)
56. Sun, D., Fu, Y., Liu, W., Ye, L., Wang, D., Yang, L., Fu, X., Li, Z.: Studies on photocatalytic CO_2 reduction over NH2-Uio-66 (Zr) and its derivatives: towards a better understanding of photocatalysis on metal–organic frameworks. Chem. Eur. J. **19**, 14279–14285 (2013)
57. Yan, Z.H., Du, M.H., Liu, J., Jin, S., Wang, C., Zhuang, G.L., Kong, X.J., Long, L.S., Zheng, L.S.: Photo-generated dinuclear $\{Eu(II)\}_2$ active sites for selective CO_2 reduction in a photosensitizing metal-organic framework. Nat. Commun. **9**, 3353 (2018)
58. Ye, L., Gao, Y., Cao, S., Chen, H., Yao, Y., Hou, J., Sun, L.: Assembly of highly efficient photocatalytic CO_2 conversion systems with ultrathin two-dimensional metal–organic framework nanosheets. Appl. Catal. B-Environ. **227**, 54–60 (2018)
59. Yan, S., Yu, Y., Cao, Y.: Synthesis of porous $ZnMn_2O_4$ flower-like microspheres by using MOF as precursors and its application on photoreduction of CO_2 into CO. Appl. Surf. Sci. **465**, 383–388 (2019)

60. Han, Y., Xu, H., Su, Y., Xu, Z.L., Wang, K., Wang, W.: Noble metal (Pt, Au@ Pd) nanoparticles supported on metal organic framework (MOF-74) nanoshuttles as high-selectivity CO_2 conversion catalysts. J. Catal. **370**, 70–78 (2019)
61. Zhao, J., Wang, Q., Sun, C., Zheng, T., Yan, L., Li, M., Shao, K., Wang, X., Su, Z.: A hexanuclear cobalt metal–organic framework for efficient CO_2 reduction under visible light. J. Mater. Chem. A. **5**, 12498–12505 (2017)
62. Hong, Q.L., Zhang, H.X., Zhang, J.: Synthesis of boron imidazolate frameworks with cobalt clusters for efficient visible-light driven CO_2 reduction. J. Mater. Chem. A. **7**, 17272–17276 (2019)
63. Xu, Y., Mo, J., Xie, G., Ding, D., Ding, S., Wang, X., Li, C.: MOF-derived Co1.11Te2 with half-metallic characteristic for efficient photochemical conversion of CO_2 under visible-light irradiation. Chem. Commun. **55**, 6862–6865 (2019)
64. Han, B., Ou, X., Deng, Z., Song, Y., Tian, C., Deng, H., Xu, Y.J., Lin, Z.: Nickel metal-organic framework monolayers for photoreduction of diluted CO_2: metal-node-dependent activity and selectivity. Angew. Chem. Int. Edn. **57**, 16811–16815 (2018)
65. Zhu, W., Zhang, C., Li, Q., Xiong, L., Chen, R., Wan, X., Wang, Z., Chen, W., Deng, Z., Peng, Y.: Selective reduction of CO_2 by conductive MOF nanosheets as an efficient co-catalyst under visible light illumination. Appl. Catal. B Environ. **238**, 339–345 (2018)
66. Meng, J., Chen, Q., Lu, J., Liu, H.: Z-scheme photocatalytic CO_2 reduction on a heterostructure of oxygen-defective ZnO/reduced graphene Oxide/UiO-66-NH2 under visible light. ACS Appl. Mater. Interfaces **11**, 550–562 (2018)
67. Crake, A., Christoforidis, K.C., Kafizas, A., Zafeiratos, S., Petit, C.: CO_2 capture and photocatalytic reduction using bifunctional TiO_2/MOF nanocomposites under UV–vis irradiation. Appl. Catal. B- Environ. **210**, 131–140 (2017)
68. Xie, Y., Fang, Z., Li, L., Yang, H., Liu, T.F.: Creating chemisorption sites for enhanced CO_2 photoreduction activity through alkylamine modification of MIL-101-Cr. ACS Appl. Mater. Interfaces **11**, 27017–27023 (2019)
69. Wang, X.K., Liu, J., Zhang, L., Dong, L.Z., Li, S.L., Kan, Y.H., Li, D.S., Lan, Y.Q.: Monometallic catalytic models hosted in stable metal–organic frameworks for tunable CO_2 photoreduction. ACS Catal. **9**, 1726–1732 (2019)
70. Wang, S., Serre, C.: Toward green production of water-stable metal–organic frameworks based on high-valence metals with low toxicities. ACS Sustain. Chem. Eng. **7**(14), 11911–11927 (2019)
71. Li, J., Musho, T., Bright, J., Wu, N.: Functionalization of a metal–organic framework semiconductor for tuned band structure and catalytic activity. J. Electrochem. Soc. **166**(5), H3029–H3034 (2019)
72. Laurier, K.G.M., Vermoortele, F., Ameloot, R., De Vos, D.E., Hofkens, J., Roeffaers, M.B.J.: Iron(III)-based metal–organic frameworks as visible light photocatalysts. J. Am. Chem. Soc. **135**(39), 14488–14491 (2013)
73. Dao, X.Y., Guo, J.H., Zhang, X.Y., Wang, S.Q., Chengm, X.M., Sun, W.Y.: Structure-dependent iron-based metal–organic frameworks for selective CO_2-to-CH_4 photocatalytic reduction. J. Mater. Chem. A **8**, 25850–25856 (2020)
74. Wang, D., Huang, R., Liu, W., Sun, D., Li, Z.: Fe-based MOFs for photocatalytic CO_2 reduction: role of coordination unsaturated sites and dual excitation pathways. ACS Catal. **4**(12), 4254–4260 (2014)
75. Li, Y., et al.: Effect of aluminum on the nature of the iron species in Fe-SBA-15. J. Phys. Chem. B **110**, 26114–26121 (2006)
76. Zhang, Z., Li, X., Liua, B., Zhao, Q., Chen, G.: Hexagonal microspindle of NH_2-MIL-101(Fe) metal–organic frameworks with visible-light-induced photocatalytic activity for the degradation of toluene. RSC Adv. **6**, 4289–4295 (2016)
77. Nishikawa, M., Mitani, Y., Nosaka, Y.: Photocatalytic reaction mechanism of Fe(III)-grafted TiO_2 studied by means of ESR spectroscopy and chemiluminescence photometry. J. Phys. Chem. C **116**, 14900–14907 (2012)
78. Yu, Q., Meng, X., Wang, G.T., Li, P., Ye, J.H.: Hematite films decorated with nanostructured ferric oxyhydroxide as photoanodes for efficient and stable photoelectrochemical water splitting. Adv. Funct. Mater. **25**, 2686–2692 (2015)
79. Chen, E.X., Xu, G., Lin, Q.P.: Robust porphyrin-spaced zirconium–pyrogallate frameworks with high proton conduction. Inorg. Chem. **58**, 3569–3573 (2019)
80. Wu, L.Y., Mu, Y.F., Guo, X.X., Zhang, W., Zhang, Z.M., Zhang, M., Lu, T.B.: Encapsulating perovskite quantum dots in iron-based metal–organic frameworks (MOFs) for efficient photocatalytic CO_2 reduction. Angew. Chem. Inter. Edn. **58**(28), 9491–9495 (2019)
81. Bai, Y., Dou, Y., Xie, L.H., Rutledge, W., Li, J.R., Zhou, H.C.: Zr-based metal–organic frameworks: design, synthesis, structure, and applications. Chem. Soc. Rev. **45**, 2327–2367 (2016)
82. Vahabi, A.H., Norouzi, F., Sheibani, E., Nasrabadi, M.R.: Functionalized Zr-UiO-67 metal-organic frameworks: structural landscape and application. Coord. Chem. Rev. **445**(15), 214050 (2021)
83. Gao, X., Guo, B., Guo, C., Meng, Q., Liang, J., Liu, J.: Zirconium-based metal–organic framework for efficient photocatalytic reduction of CO_2 to CO: the influence of doped metal ions. ACS Appl. Mater. Interfaces **12**(21), 24059–24065 (2020)
84. Sun, M., et al.: Enhancement of visible-light-driven CO_2 reduction performance using an amine-functionalized zirconium metal–organic framework. Dalton Trans. **47**, 909–915 (2018)
85. Dashu, C., Hongzhu, X., Chungang, W., Zhongmin, S.: Highly efficient visible-light-driven CO_2 reduction to formate by a new anthracene-based zirconium MOF via dual catalytic routes. J. Mater. Chem. A **4**, 2657–2662 (2016)
86. Dai, S., et al.: Ultrasmall copper nanoclusters in zirconium metal-organic frameworks for the photoreduction of CO_2. Angew. Chem. Inter. Edn. **62**(14), e202211848 (2022)
87. Osterrieth, J.W.M., et al.: Core–shell gold Nanorod@Zirconium-based metal–organic framework composites as in situ size-selective Raman probes. J. Am. Chem. Soc. **141**, 3893–3900 (2019)
88. Jin, R.C.: Atomically precise metal nanoclusters: stable sizes and optical properties. Nanoscale **7**, 1549–1565 (2015)
89. Sonowal, K., Nandal, N., Basyach, P., Lalita, L., Jain, S.L., Saikia, L.: Photocatalytic reduction of CO_2 to methanol using Zr(IV)-based MOF composite with g-C3N4 quantum dots under visible light irradiation. J. CO_2 Util. **57**, 101905 (2022)
90. Wang, S.Q., Gu, X., Wang, X., Zhang, X.Y., Dao, X.Y., Cheng, X.M., Ma, J., Sun, W.Y.: Defect-engineering of Zr(IV)-based metal-organic frameworks for regulating CO_2 photoreduction. Chem. Eng. J. **429**(1), 132157 (2022)
91. Fu, Y., Sun, D., Chen, Y., Huang, R., Ding, Z., Fu, X., Li, Z.: An amine-functionalized titanium metal–organic framework photocatalyst with visible-light-induced activity for CO_2 reduction. Angew. Chem. Inter. Edn. **51**(14), 3364–3367 (2012)
92. Zheng, Y.L., Dai, M.D., Yang, X.F., Yin, H.J., Zhang, Y.W.: Copper(II)-doped two-dimensional titanium-based metal–organic frameworks toward light-driven CO_2 reduction to value-added products. Inorg. Chem. **61**(35), 13981–13991 (2022)
93. Cheng, X.M., Dao, X.Y., Wang, S.Q., Zhao, J., Sun, W.Y.: Enhanced photocatalytic CO_2 reduction activity over NH_2-MIL-125(Ti) by facet regulation. ACS Catal. **11**, 650–658 (2021)
94. Li, N., Liu, X., Zhou, J., Chen, W., Liu, M.: Encapsulating CuO quantum dots in MIL-125(Ti) coupled with g-C_3N_4 for efficient photocatalytic CO_2 reduction. Chem. Eng. J. **399**, 125782–125792 (2020)

95. Zhao, Y., Cai, W., Chen, J., Miao, Y.Y., Bu, Y.: A highly efficient composite catalyst constructed from NH_2-MIL-125(Ti) and reduced graphene oxide for CO_2 photoreduction. Front. Chem. **7**, 789 (2019)
96. Wang, S., et al.: A robust titanium isophthalate metal–organic framework for visible-light photocatalytic CO_2 methanation. Chem **6**, 3409–3427 (2020)
97. Chen, S., Yang, F., Gao, H., Wang, J., Chen, X., Zhang, X., Li, J., Li, A.: Construction of dual ligand Ti-based MOFs with enhanced photocatalytic CO_2 reduction performance. J. CO_2 Util. **48**, 101528 (2021)
98. Ibanez, A.A., et al.: Metal–organic aerogels based on titanium(IV) for visible-light conducted CO_2 photoreduction to alcohols. Mater. Today Energ. **30**, 101178 (2022)
99. Syzgantseva, M.A., Ireland, C.P., Ebrahim, F.M., Smit, B., Syzgantseva, O.A.: Metal substitution as the method of modifying electronic structure of metal–organic frameworks. J. Am. Chem. Soc. **141**(15), 6271–6278 (2019)
100. Wang, C.C., Du, X.D., Li, J., Guo, X.X., Wang, P., Zhang, J.: Photocatalytic Cr(VI) reduction in metal-organic frameworks: a mini-review. Appl. Catal. B Environ. **193**, 198–216 (2016)
101. Lee, Y., Kim, S., Kang, J.K., Cohen, S.M.: Photocatalytic CO_2 reduction by a mixed metal (Zr/Ti), mixed ligand metal–organic framework under visible light irradiation. Chem. Commun. **51**(26), 5735–5738 (2015)
102. Sun, D., Liu, W., Qiu, M., Zhang, Y., Li, Z.: Introduction of a mediator for enhancing photocatalytic performance via post-synthetic metal exchange in metal–organic frameworks (MOFs). Chem. Commun. **51**(11), 2056–2059 (2015)
103. Robatjazi, H., et al.: Metal–organic frameworks tailor the properties of aluminum nanocrystals. Sci. Adv. **5**, 1–10 (2019)
104. Verma, R., Belgamwar, R., Polshettiwar, V.: Plasmonic photocatalysis for CO_2 conversion to chemicals and fuels. ACS Materials Lett. **3**(5), 574–598 (2021)
105. Luna, R.R.: Visible-light-harvesting basolite-A520 metal organic framework for photocatalytic hydrogen evolution. Microporous Mesoporous Mater. **355**, 112565 (2023)
106. Duma, Z.G., Moma, J., Langmi, H.W., Louis, B., Parkhomenko, K., Musyoka, N.M.: Towards high CO_2 conversions using Cu/Zn catalysts supported on aluminum fumarate metal-organic framework for methanol synthesis. Catalysts **12**, 1104 (2022)
107. Logan, M.W., Adamson, J.D., Le, D., Romo, F.J.U.: Structural stability of N-Alkyl-functionalized titanium metal–organic frameworks in aqueous and humid environments. ACS Appl. Mater. Interfaces **9**(51), 44529–44533 (2017)
108. Xin, X., et al.: Hydrophobic polyoxometalate-based metal–organic framework for efficient CO_2 photoconversion. ACS Appl. Mater. Interfaces **11**(29), 25790–25795 (2019)
109. Lin, C., et al.: Porphyrin-based metal–organic frameworks for efficient photocatalytic H_2 production under visible-light irradiation. Inorg. Chem. **60**(6), 3988–3995 (2021)
110. Yusuf, V.F., Malek, N.I., Kailasa, S.K.: Review on metal−organic framework classification, synthetic approaches, and influencing factors: applications in energy, drug delivery, and wastewater treatment. ACS Omega **7**, 44507–45531 (2022)
111. Joseph, J., Iftekhar, S., Srivastava, V., Fallah, Z., Zare, E.N., Sillanpa, M.: Iron-based metal-organic framework: synthesis, structure and current technologies for water reclamation with deep insight into framework integrity. Chemosphere **284**, 131171 (2021)
112. Verma, P., Stewart, D.J., Raja, R.: Recent advances in photocatalytic CO_2 utilisation over multifunctional metal organic frameworks. Catalysts **10**, 1176 (2020)